

# GAMMA-RAY EMISSIONS FROM PULSARS: SPECTRA OF THE TeV FLUXES FROM OUTER GAP ACCELERATORS

K. HIROTANI

National Astronomical Observatory, Mitaka, Tokyo 181-8588, Japan; hirotoni@hotaka.mtk.nao.ac.jp

Received 1999 September 2; accepted 2000 September 7

## ABSTRACT

We study the  $\gamma$ -ray emissions from an outer magnetospheric potential gap around a rotating neutron star. Migratory electrons and positrons are accelerated by the electric field in the gap to radiate copious  $\gamma$ -rays via a curvature process. Some of these  $\gamma$ -rays materialize as pairs by colliding with the X-rays in the gap, leading to a pair production cascade. Imposing the closure condition that a single pair produces one pair in the gap on average, we explicitly solve the strength of the acceleration field and demonstrate how the peak energy and the luminosity of the curvature-radiated, GeV photons depend on the strength of the surface blackbody and the power-law emissions. Some predictions on the GeV emission from 12 rotation-powered pulsars are presented. We further demonstrate that the expected pulsed TeV fluxes are consistent with their observational upper limits. An implication of high-energy pulse phase width versus pulsar age, spin, and magnetic moment is discussed.

*Subject headings:* acceleration of particles — gamma rays: observations — gamma rays: theory — magnetic fields

## 1. INTRODUCTION

The EGRET experiment on the *Compton Gamma Ray Observatory* has detected pulsed signals from seven rotation-powered pulsars (Crab [Nolan et al. 1993; Fierro et al. 1998], Vela [Kanbach et al. 1994; Fierro et al. 1998], Geminga [Mayer-Hasselwander et al. 1994; Fierro et al. 1998], PSR B1706–44 [Thompson et al. 1996], PSR B1046–58 [Kaspi et al. 2000], PSR B1055–52 [Thompson et al. 1999], and PSR B1951+32 [Ramanamurthy et al. 1995]; for reviews, e.g., Ulmer 1994; Nel et al. 1996; Nolan et al. 1996), with PSR B0656+14 being a possible detection (Ramanamurthy et al. 1996). The modulation of the  $\gamma$ -ray light curves at GeV energies testifies to the production of  $\gamma$ -ray radiation in the pulsar magnetospheres either at the polar cap (Harding, Tademaru, & Esposito 1978; Daugherty & Harding 1982, 1996; Dermer & Sturmer 1994; Sturmer, Dermer, & Michel 1995; Shibata, Miyazaki, & Takahara 1998; Miyazaki & Takahara 1997; also see Scharlemann, Arons, & Fawley 1978 for the slot gap model) or at the vacuum gaps in the outer magnetosphere (Cheng, Ho, & Ruderman 1986a, 1986b, hereafter collectively CHR; Chiang & Romani 1992, 1994; Romani & Yadigaroglu 1995; Romani 1996; Zhang & Cheng 1997). Effective  $\gamma$ -ray production in a pulsar magnetosphere may be extended to the very high energy (VHE) region above 100 GeV as well; however, the predictions of fluxes by the current models of  $\gamma$ -ray pulsars are not sufficiently conclusive (e.g., Cheng 1994). Whether or not the spectra of  $\gamma$ -ray pulsars continue up to the VHE region is a question that remains one of the interesting issues of high-energy astrophysics.

In the VHE region, positive detections of radiation at a high confidence level have been reported from the direction of the Crab, B1706–44, and Vela pulsars (Bowden et al. 1993; Nel et al. 1993; Edwards et al. 1994; Yoshikoshi et al. 1997; see also Kifune 1996 for a review), by virtue of the technique of imaging Cerenkov light from extensive air showers. However, with respect to *pulsed* TeV emissions, only the upper limits have been, as a rule, obtained from these pulsars (see the references cited just above). If the

VHE emission originates in the pulsar magnetosphere, rather than the extended nebula, a significant fraction of it can be expected to show a pulsation. Therefore, the lack of *pulsed* TeV emissions provides a severe constraint on the modeling of particle acceleration zones in a pulsar magnetosphere.

In fact, in the CHR picture, the magnetosphere should be optically thick for pair production in order to reduce the TeV flux to an unobserved level by absorption. This in turn requires very high luminosities of tertiary photons in the infrared energy range. However, the required fluxes are generally orders of magnitude larger than the observed values (Usov 1994). We are therefore motivated by the need to contrive an outer gap model that produces less TeV emission with a moderate infrared luminosity.

High-energy emission from a pulsar magnetosphere, in fact, crucially depends on the acceleration electric field,  $E_{\parallel}$ , along the magnetic field lines. It was Hirotoni & Shibata (1999a, 1999b, 1999c; hereafter Papers I, II, III) and Hirotoni (2000b) who first solved the spatial distribution of  $E_{\parallel}$  together with particle and  $\gamma$ -ray distribution functions. They explicitly demonstrated that there is a stationary solution for an outer gap that is formed around the null surface at which the local Goldreich-Julian charge density

$$\rho_{\text{GJ}} = \frac{\Omega B_z}{2\pi c[1 - (\Omega \varpi/c)^2]} \quad (1)$$

vanishes, where  $B_z$  is the component of the magnetic field along the rotation axis,  $\Omega$  refers to the angular frequency of the neutron star,  $\varpi$  indicates the distance of the point from the rotation axis, and  $c$  is the speed of light. Subsequently, Hirotoni (2000a, hereafter Paper IV) investigated the  $\gamma$ -ray emission from an outer gap, by imposing a gap closure condition that a single pair produces one pair in the gap on average. He demonstrated that  $E_{\parallel}$  becomes typically less than 10% of the value assumed in CHR and that the resultant TeV flux is sufficiently less than the observational upper limit of the pulsed flux, if the outer gap is immersed in an X-ray field supplied by the blackbody radiation from the whole neutron star surface and/or from the heated polar

caps. In this paper, we develop his method for the case when a magnetospheric power-law component contributes in addition to the blackbody components.

In the next section, we formulate the gap closure condition. Solving the condition in § 3, we investigate the acceleration field and the resultant  $\gamma$ -ray emissions as a function of the X-ray field. In § 4, we further apply the theory to 12 rotation-powered pulsars and predict the absolute fluxes of TeV emission from their outer gaps. In the final section, we discuss the validity of assumptions and give some implications for pulse profiles of GeV emissions.

## 2. ELECTRODYNAMIC STRUCTURE OF THE GAP

We first describe the acceleration field in § 2.1 and then consider the energy of curvature-radiated  $\gamma$ -rays in § 2.2, the X-ray field illuminating the gap in § 2.3, and the pair production mean free path in § 2.4. We further formulate in § 2.5 the gap closure condition that one of the copious  $\gamma$ -rays emitted by a single pair materializes as a pair in the gap on average. We finally present the resultant  $\gamma$ -ray properties in §§ 2.6 and 2.7.

### 2.1. Acceleration Field in the Gap

In this paper, we consider an outer gap in the following rectilinear coordinates:  $x$  is an outwardly increasing coordinate along the magnetic field lines, while  $z$  is parallel to the rotational axis. We define  $x = 0$  to be the intersection between the last open field line and the null surface where  $B_z = 0$  (Fig. 1). If we assume that the transfield thickness of the gap is larger than the gap width along the field lines, we can neglect the  $\partial_z^2$  term compared with the  $\partial_x^2$  one in the Poisson equation for the nonrotational potential,  $\Phi$ . Then we can Taylor-expand  $\rho_{GJ}$  around  $x = 0$  to obtain

$$-\frac{d^2\Phi}{dx^2} = -4\pi Ax, \quad (2)$$

where  $A$  is the expansion coefficient of  $\rho_{GJ}$  at  $x = 0$ . Since the toroidal current flowing near the light cylinder is unknown, we simply approximate  $B_z$  with its Newtonian value. Then  $A$  is given by

$$A \equiv \frac{3\Omega\mu}{2\pi cr_0^4} \frac{1}{1 - (\Omega r_0 \sin \theta_0/c)^2} \times \left[ \frac{3}{2} \sin 2\theta_0 \cos(\theta_0 - \alpha_i) + \cos 2\theta_0 \sin(\theta_0 - \alpha_i) \right], \quad (3)$$

where  $\mu$  refers to the magnetic dipole moment of the

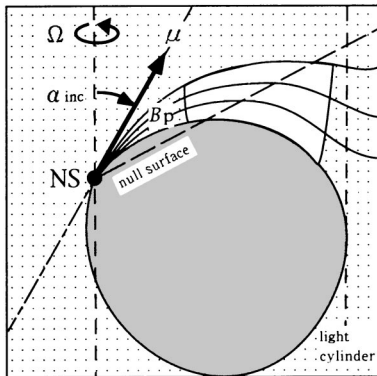


FIG. 1.—Side view of a hypothetical outer magnetospheric gap in which pair production cascade takes place.

neutron star;  $r_0$  is the distance of the gap center ( $x = 0$ ) from the neutron star, and  $\theta_0$  is the polar angle of the gap center (in the first quadrant). They are related to  $\alpha_i$  as

$$\frac{r_0}{\varpi_{LC}} \equiv \frac{\sin^2(\theta_0 - \alpha_i)}{\sin \theta_{LC} \sin^2(\theta_{LC} - \alpha_i)} \quad (4)$$

and

$$\tan \theta_0 \equiv \frac{3 \tan \alpha_i + \sqrt{9 \tan^2 \alpha_i + 8}}{2}, \quad (5)$$

where the light cylinder radius is defined by

$$\varpi_{LC} = \frac{c}{\Omega} = 3.0 \times 10^8 \Omega_2^{-1} \text{ cm} \quad (6)$$

and the colatitude angle  $\theta_{LC}$  at which the last-open field line intersects with the light cylinder is implicitly solved from

$$2 \cot(\theta_{LC} - \alpha_i) \sin \theta_{LC} + \cos \theta_{LC} = 0; \quad (7)$$

$\Omega_2 \equiv \Omega/10^2 \text{ rad s}^{-1}$ . For the order of magnitude,  $A \sim \rho_{GJ}/\varpi_{LC}$  holds. Its exact values are  $3.19 \times 10^{-12} \Omega_2^5 \mu_{30}$  esu for  $\alpha_i = 30^\circ$  and  $1.22 \times 10^{-11} \Omega_2^5 \mu_{30}$  esu for  $\alpha_i = 45^\circ$ , where  $\mu_{30} \equiv \mu/10^{30} \text{ G cm}^3$ .

Integrating equation (2), we obtain the acceleration field  $E_{||}(x) \equiv -d\Phi/dx = E_{||}(0) - 2\pi Ax^2$ , where  $E_{||}(0)$  refers to the value of  $E_{||}$  at  $x = 0$ . Defining the boundaries of the gap to be the places where  $E_{||}$  vanishes, we obtain  $E_{||}(0) = 2\pi AH^2$ . It is noteworthy that the nonvanishment of  $dE_{||}/dx$  at  $x = \pm H$  is consistent with the stability condition at the plasma-vacuum interface if the electrically supported magnetospheric plasma is completely charge separated, i.e., if the plasma cloud at  $x < -H$  is composed of electrons alone (Krause-Polstorff & Michel 1985a, 1985b). We assume that the Goldreich-Julian plasma gap boundary is stable with  $E_{||} = 0$  on the boundary,  $x = -H$ .

We can now evaluate the typical strength of  $E_{||}$  by averaging its values throughout the gap as follows:

$$\begin{aligned} \bar{E}_{||} &= \frac{1}{H} \int_0^H dx [E_{||}(0) - 2\pi Ax^2] \\ &= \frac{4}{3} \pi AH^2. \end{aligned} \quad (8)$$

We shall use this  $\bar{E}_{||}$  as a representative value of the acceleration field in the gap. Defining the nondimensional gap width  $h \equiv H/\varpi_{LC}$  and substituting the values of  $A$ , we obtain

$$\bar{E}_{||} = C_E \Omega_2^3 \mu_{30} h^2 \text{ V m}^{-1}, \quad (9)$$

where  $C_E = 3.61 \times 10^{10}$  for  $\alpha_i = 30^\circ$  and  $1.39 \times 10^{11}$  for  $\alpha_i = 45^\circ$ .

The voltage drop in the gap is given by

$$V_{\text{gap}} = \bar{E}_{||} \times 2H = \frac{8}{3} \pi AH^3. \quad (10)$$

For an outer gap that extends to the light cylinder ( $H \sim 0.5\varpi_{LC}$ ),  $V_{\text{gap}}$  becomes as large as the available electromotive force (EMF) exerted on the spinning neutron star surface,  $V_* \approx 10^{15} (\Omega_2/0.5)^2 \mu_{30} \text{ V}$ .

### 2.2. Energy of Curvature-radiated $\gamma$ -Rays

The most effective assumption for the particle motion in the gap arises from the fact that the velocity saturates immediately after the birth of the particles in the balance between the radiation reaction force and the electric force.

The reaction force is mainly due to curvature radiation if the gap is immersed in a moderate X-ray field. Equating the electric force  $eE_{\parallel}$  and the radiation reaction force, we obtain the Lorentz factor of saturated particles as follows:

$$\bar{\Gamma} = \left( \frac{3R_c^2 \bar{E}_{\parallel}}{2e} \right)^{1/4}, \quad (11)$$

where  $R_c$  and  $e$  refer to the curvature radius of the magnetic field line and the magnitude of the charge on the electron.  $\bar{\Gamma}$  is related to  $h \equiv H/\varpi_{LC}$  by

$$\bar{\Gamma} = C_{\Gamma} R_{0.5}^{1/2} (\Omega_2 \mu_{30})^{1/4} h^{1/2}, \quad (12)$$

where  $C_{\Gamma} = 9.59 \times 10^7$  for  $\alpha_i = 30^\circ$  and  $1.34 \times 10^9$  for  $\alpha_i = 45^\circ$ ;  $R_{0.5} \equiv R_c/(0.5\varpi_{LC})$ .

However, if the gap width  $H$  is less than the length scale for the particles to be accelerated up to  $\bar{\Gamma}$ , the typical Lorentz factor should be rather estimated by  $eE_{\parallel} H/m_e c^2$  because typical particles are accelerated by the potential  $V_{\text{gap}}/2 = E_{\parallel} H$ . Therefore, we can evaluate the Lorentz factor as

$$\Gamma = \min(\bar{\Gamma}, eE_{\parallel} H/m_e c^2). \quad (13)$$

Using this  $\Gamma$ , we obtain the central energy of curvature radiation,

$$E_c = \frac{3\Gamma^3}{2} \frac{\hbar c}{R_c}, \quad (14)$$

where  $\hbar$  is the Planck constant divided by  $2\pi$ . In this paper, we adopt the gray approximation in the sense that all the  $\gamma$ -rays are radiated at energy  $E_c$ . In the final section of Paper IV, we demonstrated that this gray approximation gave a good estimate of the gap width and other quantities describing the gap, by comparing them with those obtained in the nongray cases in which the Boltzmann equations of particles and  $\gamma$ -rays were solved together with the Poisson equation for  $\Phi$ .

### 2.3. X-Ray Field

Before proceeding to the discussion on pair production mean free path, it is desirable to describe the X-ray field that illuminates the outer gap. The X-ray field of a rotation-powered neutron star within the light cylinder can be attributed to the following three emission processes: (1) photospheric emission from the whole surface of a cooling neutron star (Greenstein & Hartke 1983; Romani 1987; Shibano et al. 1992; Pavlov et al. 1994; Zavlin et al. 1995a), (2) thermal emission from the neutron star's polar caps, which are heated by the bombardment of relativistic particles streaming back to the surface from the magnetosphere (Kundt & Schaaf 1993; Zavlin, Shibano, & Pavlov 1995b; Gil & Krawczyk 1997), and (3) nonthermal emission from relativistic particles accelerated in the pulsar magnetosphere (Ochelkov & Usov 1980a, 1980b; El-Gowhari & Arponen 1972; Aschenbach & Brinkmann 1975; Hardee & Rose 1974; Daishido 1975).

The spectrum of the first component is expected to be expressed with a modified blackbody. However, for simplicity, we approximate it in terms of a Planck function with temperature  $kT_s$  because the X-ray spectrum is occasionally fitted by a simple blackbody spectrum. We regard a blackbody component as the first one if its observed emitting area is comparable to the whole surface of a neutron star,  $A_* \equiv 4\pi r_*^2$ , where  $r_*$  denotes the neutron star radius. We

take account of both the pulsed and the nonpulsed surface blackbody emission as this soft blackbody component.

As for the second component, we regard a blackbody component as the heated polar cap emission if its observed emitting area is much smaller than  $A_*$ . We approximate its spectrum by a Planck function. We take account of both the pulsed and the nonpulsed polar cap emission as this hard blackbody component.

Unlike the first and the second components, a power-law component is usually dominated by a nebula emission. To get rid of the nebula emission, which illuminates the outer gap inefficiently, we adopt only the pulsed components of a power-law emission as the third component.

### 2.4. Pair Production Mean Free Path

In this subsection, we draw attention to how the pair production mean free path is related to the X-ray field described in the previous section. To this end, we first give the threshold energy for X-ray photons to materialize. Then, we consider the mean free path for a  $\gamma$ -ray photon to materialize as a pair in a collision with one of the soft blackbody X-rays in § 2.4.2, the hard blackbody ones in § 2.4.3, and the magnetospheric, power-law X-rays in § 2.4.4. We finally summarize how the real mean free path should be computed under the existence of these three X-ray components in § 2.4.5.

#### 2.4.1. Threshold Energy

The threshold energy for a soft photon to materialize as a pair in a collision with the  $\gamma$ -ray having energy  $m_e c^2 \epsilon_{\gamma} = E_c$  is given by

$$E_{\text{th}} = \frac{2}{1 - \cos \phi_{ab} \cos \theta_c} \frac{m_e c^2}{\epsilon_{\gamma}}, \quad (15)$$

where  $\cos \phi_{ab} \cos \theta_c$  refers to the cosine of the three-dimensional collisional angle between the X-ray and the  $\gamma$ -ray. The lower bound of  $2/(1 - \cos \phi_{ab} \cos \theta_c)$  is unity, which is realized if the two photons collide head-on.

To evaluate  $\cos \phi_{ab} \cos \theta_c$ , we must consider the  $\gamma$ -ray's toroidal momenta due to aberration. At the gap center, the aberration angle  $\phi_{ab}$  is given by  $\sin^{-1}(r_0 \sin \theta_0 / \varpi_{LC})$ . In the case of  $\alpha_i = 30^\circ$ , we obtain  $\phi_{ab} = 20.4^\circ$ . The collisional angle on the poloidal plane becomes  $\theta_c = 90^\circ - \theta_0 = 21.6^\circ$  (or  $\theta_c = 90^\circ + \theta_0 = 158.4^\circ$ ) for outwardly (or inwardly) propagating  $\gamma$ -rays, where  $\theta_0$  is computed from equation (5). Therefore, we obtain  $\cos \phi_{ab} \cos \theta_c = \pm 0.855$ , where the upper and the lower signs correspond to the outwardly and inwardly propagating  $\gamma$ -rays, respectively. On the other hand, in the case of  $\alpha_i = 45^\circ$ , we have  $\phi_{ab} = 14.0^\circ$  and  $\theta_c = 15.6^\circ$  (or  $\theta_c = 164.3^\circ$ ) to obtain  $\cos \phi_{ab} \cos \theta_c = \pm 0.923$ .

#### 2.4.2. Soft Blackbody Component

We first consider the pair production mean free path,  $\lambda_s$ , for a  $\gamma$ -ray photon to materialize in a collision with one of the soft blackbody X-rays. In a realistic outer gap, both the outwardly and inwardly propagating  $\gamma$ -rays contribute for  $\lambda_s$ . Therefore,  $\lambda_s$  is given by an arithmetic average of these two contributions as follows (Paper IV; see also eq. [3.1] in Blandford & Levinson 1995 for the factor  $1 \pm \mu_c$ ):

$$\begin{aligned} \frac{1}{\lambda_s} \equiv & \kappa(1 - \mu_c) \int_{2/(1 - \mu_c)}^{\infty} \epsilon_{\gamma}^{\infty} d\epsilon_X \frac{dN_s}{d\epsilon_X} \sigma_p(\epsilon_{\gamma}, \epsilon_X, \mu_c) \\ & + (1 - \kappa)(1 + \mu_c) \int_{2/(1 + \mu_c)}^{\infty} \epsilon_{\gamma}^{\infty} d\epsilon_X \frac{dN_s}{d\epsilon_X} \sigma_p(\epsilon_{\gamma}, \epsilon_X, -\mu_c), \end{aligned} \quad (16)$$

where  $\mu_c \equiv |\cos \phi_{ab} \cos \theta_c|$ ; the pair production cross section is given by (Berestetskii, Lifshitz, & Pitaevskii 1989)

$$\sigma_p(\epsilon_\gamma, \epsilon_X, \mu_c) \equiv \frac{3}{16} \sigma_T (1 - v^2) \times \left[ (3 - v^4) \ln \frac{1+v}{1-v} - 2v(2 - v^2) \right],$$

$$v(\epsilon_\gamma, \epsilon_X, \mu_c) \equiv \sqrt{1 - \frac{2}{1 - \mu_c} \frac{1}{\epsilon_\gamma \epsilon_X}}, \quad (17)$$

where  $\sigma_T$  is the Thomson cross section and  $\epsilon_X \equiv E_X/m_e c^2$  refers to the dimensionless energy of an X-ray photon. We may notice here that the nondimensional threshold energy ( $E_{th}/m_e c^2$ ) appears in the lower bound of the integral in equation (16).

When a blackbody emission dominates the X-ray field,  $H$  occasionally becomes as large as  $0.3\varpi_{LC}$ . In this case, we must take the dilution effect of the surface radiation into account. The number density of the soft X-rays between energies  $m_e c^2 \epsilon_X$  and  $m_e c^2(\epsilon_X + d\epsilon_X)$  at position  $x$  is given by

$$\frac{dN_s}{d\epsilon_X} = \left[ 1 + 2 \sin \theta_0 \frac{x}{\varpi_{LC}} + \left( \frac{x}{\varpi_{LC}} \right)^2 \right]^{-1} \left( \frac{dN_s}{d\epsilon_X} \right)_0. \quad (18)$$

Here, the number density at the gap center is given by the Planck law

$$\left( \frac{dN_s}{d\epsilon_X} \right)_0 = \frac{1}{4\pi^2} \left( \frac{m_e c^2}{\hbar} \right)^3 \left( \frac{A_s}{4\pi r_0^2} \right) \frac{\epsilon_X^2}{\exp(\epsilon_X/\Delta_s) - 1}, \quad (19)$$

where  $A_s$  indicates the observed emission area of the soft blackbody;  $\Delta_s$  is defined by

$$\Delta_s \equiv \frac{kT_s}{m_e c^2}, \quad (20)$$

where  $kT_s$  refers to the soft blackbody temperature measured by a distant observer. Since the outer gap is located outside of the deep gravitational potential well of the neutron star, the photon energy there is essentially the same as the distant observer measures.

The first (or the second) term in equation (16) represents the contribution from the outwardly (or inwardly) propagating  $\gamma$ -rays; for  $\alpha_i = 30^\circ$ , we adopt  $\mu_c = 0.855$ , whereas, for  $45^\circ$ ,  $\mu_c = 0.923$ . The weight  $\kappa$  reflects the ratio of the fluxes between the outwardly and inwardly propagating  $\gamma$ -rays. For example, if  $\kappa$  were to be 1.0, only outwardly propagating  $\gamma$ -rays would contribute for the pair production. From Paper III, we know that the flux of the outwardly propagating  $\gamma$ -rays is typically about 10 times larger than that of the inwardly propagating ones. In what follows, we thus adopt  $\kappa = 0.9$ . This value of  $\kappa$  was justified in the final section of Paper IV.

#### 2.4.3. Hard Blackbody Component

In this subsection, let us consider the case when the X-ray field is dominated by the *hard* blackbody component. In the same manner as the soft blackbody component, the *hard* blackbody component gives the following mean free path

for pair production:

$$\frac{1}{\lambda_h} \equiv \kappa(1 - \mu_c) \int_{2/(1-\mu_c)}^{\infty} \epsilon_\gamma d\epsilon_X \frac{dN_h}{d\epsilon_X} \sigma_p(\epsilon_\gamma, \epsilon_X, \mu_c) + (1 - \kappa)(1 + \mu_c) \int_{2/(1+\mu_c)}^{\infty} \epsilon_\gamma d\epsilon_X \times \frac{dN_h}{d\epsilon_X} \sigma_p(\epsilon_\gamma, \epsilon_X, -\mu_c), \quad (21)$$

where  $\mu_c$  takes the same value as the soft blackbody-dominated case and  $\kappa = 0.9$ . The number density of the hard blackbody X-rays between energies  $m_e c^2 \epsilon_X$  and  $m_e c^2(\epsilon_X + d\epsilon_X)$  at position  $x$  is given by

$$\frac{dN_h}{d\epsilon_X} = \left[ 1 + 2 \sin \theta_0 \frac{x}{\varpi_{LC}} + \left( \frac{x}{\varpi_{LC}} \right)^2 \right]^{-1} \left( \frac{dN_h}{d\epsilon_X} \right)_0, \quad (22)$$

$$\left( \frac{dN_h}{d\epsilon_X} \right)_0 = \frac{1}{4\pi^2} \left( \frac{m_e c^2}{\hbar} \right)^3 \left( \frac{A_h}{4\pi r_0^2} \right) \frac{\epsilon_X^2}{\exp(\epsilon_X/\Delta_h) - 1}, \quad (23)$$

where  $A_h$  denotes the observed emission area of the hard blackbody emission. The quantity  $\Delta_h$  is defined by

$$\Delta_h \equiv \frac{kT_h}{m_e c^2}, \quad (24)$$

where  $kT_h$  refers to the hard blackbody temperature measured by a distant observer.

#### 2.4.4. Power-Law Component

Since the secondary photons emitted outside of the gap via synchrotron process will be beamed in the same direction as the primary  $\gamma$ -rays, the typical collision angle on the poloidal plane can be approximated as  $h \equiv H/\varpi_{LC}$  rad. It follows that the mean free path corresponding to the power-law emission becomes

$$\frac{1}{\lambda_{pl}} = (1 - \mu_c) \int_{\zeta/\epsilon_\gamma}^{\infty} d\epsilon_X \frac{dN_{pl}}{d\epsilon_X} \sigma_p(\epsilon_\gamma, \epsilon_X, \mu_c), \quad (25)$$

where

$$\zeta \equiv \frac{2}{1 - \mu_c}; \quad (26)$$

$dN_{pl}/d\epsilon_X$  refers to the number density of the power-law X-rays between energies  $m_e c^2 \epsilon_\gamma$  and  $m_e c^2(\epsilon_\gamma + d\epsilon_\gamma)$ ; we adopt

$$\mu_c = \cos \left( \frac{H}{r_0 \sin \theta_0} \phi_{ab} \right) \cos h \quad (27)$$

for the power-law component. We may notice here that both the  $\gamma$ -rays and the magnetospheric, power-law X-rays suffer aberration and that the resultant collision angle in the azimuthal direction is less than  $\phi_{ab}$  and can be assumed to be  $(H/r_0 \sin \theta_0) \phi_{ab}$ . The dependence of  $dN_{pl}/d\epsilon_X$  on  $x$  is unknown. We thus simply assume that it is constant throughout the gap and specify the form as

$$\frac{dN_{pl}}{d\epsilon_X} = N_{pl} \epsilon_X^\alpha \quad (\epsilon_{\min} < \epsilon_X < \epsilon_{\max}). \quad (28)$$

The photon index  $\alpha$  is typically between  $-2$  and  $-1$  for a pulsed, power-law X-ray component in the hard X-ray band (e.g., Saito 1998).

#### 2.4.5. Pair Production Mean Free Path

The true mean path,  $\lambda_p$ , is determined by the component that dominates the X-ray field, or equivalently, the smallest one among  $\lambda_s$ ,  $\lambda_h$ , and  $\lambda_{pl}$ . Therefore, we can reasonably evaluate  $\lambda_p$  as

$$\frac{1}{\lambda_p} = \frac{1}{\lambda_s} + \frac{1}{\lambda_h} + \frac{1}{\lambda_{pl}}. \quad (29)$$

When a pulsar is young, the third term will dominate because of its strong magnetospheric emission. As the pulsar evolves, the first term will become dominant owing to the diminishing magnetospheric emission. As the pulsar evolves further, polar cap heating due to particle bombardment begins to dominate; therefore, the second term becomes important.

#### 2.5. Gap Closure

The gap width  $2H$  is adjusted so that a single pair produces copious  $\gamma$ -ray photons (of number  $N_\gamma$ ), one of which materializes as a pair on average. Since a typical  $\gamma$ -ray photon runs the length  $H$  in the gap before escaping from either of the boundaries, the probability of a  $\gamma$ -ray photon materializing within the gap,  $N_\gamma^{-1}$ , must coincide with the optical depth for absorption,  $H/\lambda_p$ . Considering the position dependence of  $\lambda_p$  on  $x$ , we obtain

$$\frac{1}{N_\gamma} = \frac{1}{2} \int_{-H}^H \frac{dx}{\lambda_p}, \quad (30)$$

where

$$N_\gamma \approx \frac{H}{c} \frac{4e^2\Gamma}{9\hbar R_c}. \quad (31)$$

Here,  $\lambda_p$  is given by equation (29). Equation (31) is derived as follows: a single  $e^+$  or  $e^-$  emits  $\gamma$ -rays at the rate  $P = 2ce^2\Gamma^4/(3R_c^2)$ . Dividing  $P$  by the averaged photon energy,  $3\Gamma^3\hbar c/(2R_c)$ , we can estimate the number of  $\gamma$ -rays emitted per unit time by a single  $e^+$  or  $e^-$ ,  $\dot{N}_\gamma$ . Noting that a typical particle runs length  $H$  in the gap on average, we obtain  $N_\gamma = (H/c)\dot{N}_\gamma$ , which reduces to equation (31).

Substituting equations (18), (22), and (29) into equation (30), we obtain the gap closure condition

$$\frac{1}{N_\gamma} = \left( \frac{H}{\lambda_{s,0}} + \frac{H}{\lambda_{h,0}} \right) I(h) + \frac{H}{\lambda_{pl}}, \quad (32)$$

where  $\lambda_{s,0}$  and  $\lambda_{h,0}$  refer to the values of  $\lambda_s$  and  $\lambda_h$  at  $x = 0$  and

$I(h)$

$$\equiv \frac{\tan^{-1}(\tan \theta_0 + h \sec \theta_0) - \tan^{-1}(\tan \theta_0 - h \sec \theta_0)}{2h \cos \theta_0}. \quad (33)$$

For a very thin gap ( $h = H/\varpi_{LC} \ll 1$ ),  $I(h)$  approaches unity. When the surface blackbody components dominate the X-ray field,  $h$  can be as large as 0.3; as a result, the  $r^{-2}$  variation of the X-ray density becomes important. We take account of this effect in the function  $I(h)$ . When the power-law component dominates, on the other hand,  $h \ll 1$  is usually satisfied (see discussion in § 4.3); therefore, we evaluate only the X-ray density at the gap center in equation (32). Combining equations (31) and (32) and representing  $\Gamma$ ,  $\epsilon_\gamma = E_c/m_e c^2$  in terms of  $h \equiv H/\varpi_{LC}$ , we finally obtain the

equation describing  $h$  as a function of  $B_5$ ,  $\Omega_2$ ,  $kT_s$ ,  $A_s$ ,  $kT_h$ , and  $A_h$ . Once  $h$  is solved, other quantities such as  $\bar{E}_\parallel$ ,  $\Gamma$ , and  $E_c$  can be computed straightforwardly.

#### 2.6. Luminosity of GeV emissions

Let us first consider the luminosities of curvature-radiated  $\gamma$ -rays. The luminosity,  $L_{GeV}$ , can be estimated by multiplying the total number of positrons and electrons in the gap,  $N_e$ , the number of  $\gamma$ -rays emitted per particle per unit time,  $N_\gamma/(H/c)$ , and  $\gamma$ -ray energy,  $E_c$ . Supposing the conserved current density is  $\chi c \rho_{GJ} = \chi(\Omega B/2\pi e)$  and assuming that the gap exists  $\pi(H/\varpi_{LC})$  rad in the azimuthal direction, we obtain

$$N_e \sim \chi \frac{\Omega B}{2\pi c e} \times \frac{\pi H}{\varpi_{LC}} \times r_0 \sin \theta_0 \times D_\perp \times 2H, \quad (34)$$

where  $D_\perp$  is the transfield thickness of the gap on the poloidal plane. The distance of the center of the gap from the rotation axis,  $r_0 \sin \theta_0$ , becomes  $0.393\varpi_{LC}$  for  $\alpha_i = 30^\circ$  and  $0.285\varpi_{LC}$  for  $\alpha_i = 45^\circ$ . The strength of magnetic field at the gap center can be given by

$$B = 3.70 \times 10^5 \sqrt{1 + 3\cos^2(\theta_0 - \alpha_i)} \left( \frac{r_0}{\varpi_{LC}} \right)^{-3} \Omega_2^3 \mu_{30} \text{ G}. \quad (35)$$

As discussed in § 2.4 in Paper IV, we adopt  $\chi = 0.1$  and  $D_\perp = 0.3\varpi_{LC}$  as typical values in this paper.

From equations (31) and (14), we obtain

$$L_{GeV} = \frac{2}{3} \left( \chi \frac{D_\perp}{\varpi_{LC}} \right) \frac{e\Omega B r_0 \sin \theta_0}{(R_c/\varpi_{LC})^2} \Gamma^4 h^2, \quad (36)$$

where  $\Gamma$  is given by equation (13). If  $\Gamma$  is saturated, equation (11) or (12) gives

$$L_{GeV} \sim C_{GeV} \left( \chi \frac{D_\perp}{\varpi_{LC}} \right) \Omega_2^4 \mu_{30}^2 h^4 \text{ ergs s}^{-1}, \quad (37)$$

where  $C_{GeV} = 1.19 \times 10^{39}$  for  $\alpha_i = 30^\circ$  and  $1.20 \times 10^{40}$  for  $\alpha_i = 45^\circ$ .

#### 2.7. Luminosity of TeV emissions

The relativistic particles produce  $\gamma$ -rays mainly via curvature radiation as described in the preceding sections. However, even though energetically negligible, it is useful to draw attention to the TeV  $\gamma$ -rays produced via inverse Compton (IC) scatterings. Since the particles' Lorentz factor becomes  $\sim 10^{7.5}$ , it is the infrared photons with energy  $\sim 0.01$  eV that contribute most effectively as the target photons of IC scatterings. Neither the higher energy photons such as surface blackbody X-rays nor the lower energy photons such as polar cap radio emission contribute as the target photons because they have either too small cross sections or too small energy transfer when they are scattered. On these grounds, we obtain the following upper bound for the luminosity of the IC-scattered  $\gamma$ -rays:

$$L_{TeV} < 5.63 \times 10^{25} B_5 L_{30} \left( \frac{\varpi_{LC}}{r_0} \sin \theta_0 \right) \left( \chi \frac{D_\perp}{\varpi_{LC}} \right) \times \Gamma h^2 \text{ ergs s}^{-1}, \quad (38)$$

where  $L_{30}$  refers to the luminosity of infrared photons that can be scattered up to TeV energy range in units of  $10^{30}$

ergs s<sup>-1</sup>;  $B_5 \equiv B/(10^5 \text{ G})$ . The inequality comes from the fact that the scattered  $\gamma$ -rays cannot have energies greater than  $\Gamma m_e c^2$ .

The  $\nu F_\nu$  flux of IC-scattered  $\gamma$ -rays,  $(\nu F_\nu)_{\text{TeV}}$  (Jy Hz), can be readily computed as

$$(\nu F_\nu)_{\text{TeV}} = 10^{-20} \left( \frac{L_{\text{TeV}}}{\text{ergs s}^{-1}} \right) \left( \frac{\omega_{\text{TeV}}}{1 \text{ sr}} \right)^{-1} d_1^{-2} \text{ Jy Hz}, \quad (39)$$

where  $\omega_{\text{TeV}}$  refers to the solid angle in which the TeV  $\gamma$ -rays are emitted and  $d_1 \equiv d/1 \text{ kpc}$ .

An analogous relation holds for an infrared flux,  $(\nu F_\nu)_{0.01 \text{ eV}}$ , if the infrared luminosity,  $L_{0.01 \text{ eV}}$ , is emitted in a solid angle  $\omega_{0.01 \text{ eV}}$  sr. We thus obtain the flux ratio

$$\frac{(\nu F_\nu)_{\text{TeV}}}{(\nu F_\nu)_{0.01 \text{ eV}}} = 5.63 \times 10^{-5} \left( \frac{\omega_{\text{LC}}}{1 \text{ sr}} \sin \theta_0 \right) \times \Gamma \left( \chi \frac{D_\perp}{\omega_{\text{LC}}} \right) \frac{B}{10^5 \text{ G}} \frac{\omega_{0.01 \text{ eV}}}{\omega_{\text{TeV}}} h^2. \quad (40)$$

Since we take the ratio of  $\nu F_\nu$  flux at two different energies, the uncertainties arising from the distance disappear on the right-hand side. It follows from equation (40) that the order of magnitude of the ratio becomes at most  $10^3$  because  $\chi(D_\perp/\omega_{\text{LC}}) < 1$ ,  $h < 0.5$ , and  $\Gamma \sim 10^{7.5}$  hold in general.

### 3. X-RAY FIELD VERSUS $\gamma$ -RAY EMISSION

Before proceeding to an application to individual pulsars, it will be useful to investigate the general properties of  $\gamma$ -ray emission as a function of the X-ray field illuminating the gap. To this aim, we first demonstrate how the gap width  $h \equiv H/\omega_{\text{LC}}$  depends on the X-ray field in § 3.1, by solving the gap closure condition (32). We then present the energies and the luminosities of the curvature-radiated and the IC-scattered  $\gamma$ -rays in § 3.2. Throughout this section, we adopt  $\Omega_2 = 0.5$ ,  $\mu_{30} = 3.0$ ,  $A_s = A_* \equiv 4\pi r_*^2$ ,  $kT_h = 200 \text{ eV}$ ,  $\alpha = -1.5$ ,  $\epsilon_{\text{min}} = 0.1 \text{ keV}/511 \text{ keV} = 0.00020$ , and  $\epsilon_{\text{max}} = 100 \text{ keV}/511 \text{ keV} = 0.20$ .

#### 3.1. Gap Width

The results of the gap half-width divided by the light cylinder radius are presented in Figure 2. The abscissa is  $kT_s$  in eV. The model parameters of the X-ray field for the six curves are summarized in Table 1. For the three thick curves, the hard blackbody component is not included (i.e.,  $A_h = 0$ ). The thick solid, dashed, and dotted curves correspond to  $N_{\text{pl}} = 0$ ,  $10^{10}$ ,  $10^{16}$ , respectively. Therefore, the

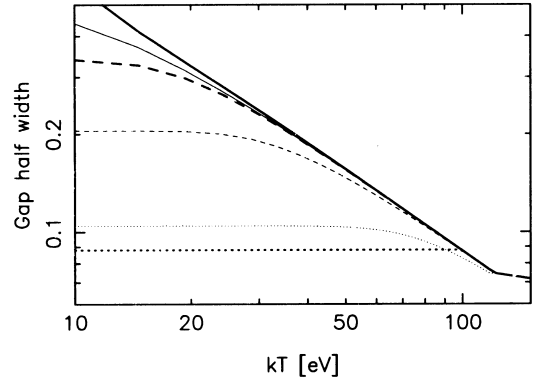


FIG. 2.—Examples of the gap half-width divided by light cylinder radius as a function of  $kT_s$  (eV). The input parameters of the X-ray field of each curve are listed in Table 1. For all six curves, pulsar parameters are fixed as  $\Omega = 50 \text{ rad s}^{-1}$ ,  $\mu = 10^{30} \text{ G cm}^3$ , and  $\alpha_i = 30^\circ$ .

thick solid curve corresponds to the least dense X-ray field, thereby giving the greatest  $h \equiv H/\omega_{\text{LC}}$  for a specific value of  $kT_s$ . For the three thin curves, on the other hand,  $N_{\text{pl}}$  is set to be 0, so that the power-law component does not contribute. The thin solid, dashed, and dotted curves correspond to  $A_h/A_* = 10^{-4}$ ,  $10^{-3}$ ,  $10^{-2}$ , respectively.

First of all, it follows from the figure that  $H$  (or equivalently  $h$  for a fixed  $\Omega$ ) is a decreasing function of  $kT_s$ . The reason is as follows. If  $kT_s$  increases, the number density of target soft photons above threshold energy  $N_s(E > E_{\text{th}})$  increases for a fixed value of  $E_{\text{th}}$ . The increased  $N_s(E > E_{\text{th}})$  results in the decrease of  $\lambda_p$ , which reduces  $H$  (eq. [32]). Accurately speaking, the reduced  $H$  results in a decrease of  $E_{\parallel}$  and hence  $E_c$ , thereby increasing  $E_{\text{th}}$ . The increased  $E_{\text{th}}$  decreases  $N_s(E > E_{\text{th}})$  to partially cancel the initial decrease of  $\lambda_p$ . In addition, the reduction of  $H$  implies the reduction of the emitting length for a particle, thereby decreasing  $N_\gamma$  and partially canceling the initial decrease of  $H$  (see eq. [32]). Nevertheless, both effects are passive; therefore, the nature of the decrease of  $H$  with increasing  $kT_s$  is unchanged.

The second thing to note is that  $h$  decreases with increasing  $A_h$ , as indicated by the three thin curves in Figure 2. This is because when  $A_h$  increases the number density of the hard blackbody component,  $N_h(E_X > E_{\text{th}})$ , increases. This in turn leads to the decrease of  $\lambda_p$ , which results in the decrease of  $h$ . If  $A_h$  is as small as  $10^{-4} A_*$  (thin solid line), the X-ray field is dominated by the power-law component only in the small  $kT_s$  range; this can be understood because the thin solid line significantly deviates from the thick solid line at  $kT_s < 30 \text{ eV}$ . However, if  $A_h$  is as large as  $10^{-2}$  (thin dotted

TABLE 1  
MODEL PARAMETERS OF X-RAY FIELD

Line	$A_s/A_*$	$kT_h$ (eV)	$A_h/A_*$	$N_{\text{pl}}$ (cm <sup>-3</sup> )	$-\alpha$	$E_{\text{min}}$ (keV)	$E_{\text{max}}$ (keV)
Thick solid .....	1.0	200	0	0	2.0	0.1	100
Thick dashed .....	1.0	200	0	$10^{10}$	2.0	0.1	100
Thick dotted .....	1.0	200	0	$10^{16}$	2.0	0.1	100
Thin solid .....	1.0	200	$10^{-4}$	0	2.0	0.1	100
Thin dashed .....	1.0	200	$10^{-3}$	0	2.0	0.1	100
Thin dotted .....	1.0	200	$10^{-2}$	0	2.0	0.1	100

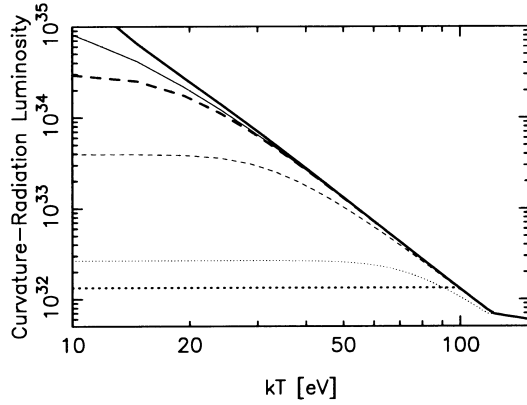


FIG. 3.—Luminosity (ergs s<sup>-1</sup>) of the curvature-radiated  $\gamma$ -rays. The abscissa represents  $kT_s$  in units of eV. The six curves correspond to the same parameter set as in Fig. 2 (or Table 1).

line), the X-ray field is dominated by the hard blackbody component up to very high  $kT_s$  ( $\sim 100$  eV).

The third thing is that  $h$  decreases with increasing  $N_{\text{pl}}$ . For a very strong magnetospheric emission (thick dotted line),  $h$  becomes not more than 0.1.

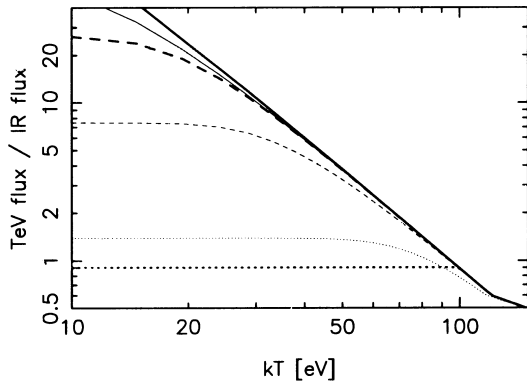


FIG. 4.—Ratio of the fluxes between TeV and infrared energy ranges. The abscissa represents  $kT_s$  in units of eV. The TeV  $\gamma$ -rays are radiated by the primary positrons and electrons in the gap via IC scatterings, while the infrared photons are presumably emitted by tertiary pairs outside of the gap via synchrotron process. The six curves correspond to the same parameter set as in Fig. 2 (or Table 1).

In short, the gap width is a decreasing function of the X-ray number density, regardless of the component that dominates the X-ray field.

### 3.2. $\gamma$ -Ray Luminosities

Let us now consider the luminosities of the curvature-radiated  $\gamma$ -rays. Substituting the results of  $h$  into equation (36), we obtain  $L_{\text{GeV}}$ ; in Figure 3, we present the results for  $\chi = 0.1$  and  $D_{\perp} = 0.3\varpi_{\text{LC}}$ . It follows from this figure that  $L_{\text{GeV}}$  is a decreasing function of the X-ray number density, regardless of the component that dominates the X-ray field. This is because the increase of the target X-ray photons results in the decreases of  $H$ .

We next present the expected ratio of the TeV and the infrared fluxes in Figure 4, by using equation (40). It follows that the  $\nu F_{\nu}$  flux of TeV emission will not exceed  $10^{11}$  Jy Hz for a typical infrared flux ( $< 10^9$  Jy Hz). Therefore, we can conclude that the pulsed TeV emission from rotation-powered pulsars cannot be detected in general by the current ground-based telescopes.

## 4. APPLICATION TO INDIVIDUAL PULSARS

In this section, we apply the theory to the 11 rotation-powered pulsars of which X-ray field at the outer gap can be deduced from observations. We first describe their X-ray and infrared fields in the next two subsections, and we present resultant GeV and TeV emissions from individual pulsars in §§ 4.3 and 4.4.

### 4.1. Input X-Ray Field

We present the observed X-ray properties of individual pulsars in order of spin-down luminosity,  $\dot{E}_{\text{rot}}$  (Table 2). We assume  $\epsilon_{\text{min}} = 0.1$  keV/511 keV and  $\epsilon_{\text{max}} = 100$  keV/511 keV for homogeneous discussion.

*Crab*.—From *HEAO 1* observations, its X-ray field is expressed by a power law with  $\alpha = -1.81 \pm 0.02$  in the primary pulse (P1) phase (Knight 1982). From the nebula and background-subtracted counting rates, the normalization factor of this power-law emission becomes  $N_{\text{pl}} = 5.3 \times 10^{15} d^2 (r_0/\varpi_{\text{LC}})^{-2}$ , where  $d$  refers to the distance in kiloparsecs.

*B0540–69*.—From *ASCA* observations in the 2–10 keV band, its X-ray radiation is known to be well fitted by a

TABLE 2  
INPUT X-RAY FIELD

Pulsar	Distance (kpc)	$\Omega$ (rad s <sup>-1</sup> )	$\log_{10} \mu$ ( $\log_{10} [\text{G cm}^3]$ )	$kT_s$ (eV)	$A_s/A_*$	$kT_h$ (eV)	$A_h/A_*$	$N_{\text{pl}}$ (cm <sup>-3</sup> )	$-\alpha$
Crab .....	2.49	188.1	30.53	...	...	...	...	$10^{17.30}$	1.8
B0540–69 .....	49.4	124.7	31.00	...	...	...	...	$10^{14.15}$	2.0
B1509–58 .....	4.40	41.7	31.19	...	...	...	...	$10^{14.04}$	1.1
J1617–5055 .....	3.30	90.6	30.78	...	...	...	...	$10^{12.64}$	1.6
J0822–4300 .....	2.20	83.4	30.53	280	0.040	...	...	...	...
Vela .....	0.50	61.3	30.53	150	0.066	...	...	...	...
B1951+32 .....	2.5	159	29.68	...	...	...	...	$10^{13.55}$	1.6
B1821–24 .....	5.1	2060	27.35	...	...	...	...	$10^{16.36}$	1.2
B0656+14 .....	0.76	15.3	30.67	67	4.5	129	$10^{-1.49}$	$10^{5.25}$	1.5
Geminga .....	0.16	26.5	30.21	48	0.16	...	...	$10^{5.00}$	1.6
B1055–52 .....	1.53	31.9	30.03	68	7.3	320	$10^{-3.64}$	...	...
J0437–4715 .....	0.180	1092	26.50	22	0.16	95	$10^{-3.28}$	...	...

power law with  $\alpha = -2.0$ . The unabsorbed luminosity in this energy range is  $1.3 \times 10^{36}$  ergs  $s^{-1}$ , which leads to  $N_{\text{pl}} = 9.0 \times 10^9 d^2 (r_0/\varpi_{\text{LC}})^{-2}$  (Saito 1998).

**B1509–58.**—From *ASCA* observations in the 2–10 keV band, its pulsed emission can be fitted by a power law with  $\alpha = -1.1$ . The unabsorbed flux in this energy range is  $2.9 \times 10^{-11}$  ergs  $\text{cm}^{-2}$   $s^{-1}$ , which leads to  $N_{\text{pl}} = 9.3 \times 10^{11} d^2 (r_0/\varpi_{\text{LC}})^{-2}$ .

**J1617–5055 and J0822–4300.**—These two pulsars have similar parameters such as  $\Omega \sim 90$  rad  $s^{-1}$ ,  $\mu \sim 10^{30.6}$  G  $\text{cm}^3$ , and characteristic age  $\tau \sim 8 \times 10^3$  yr. From the *ASCA* observations of J1617–5055 in the 3.5–10 keV band, its pulsed emission subtracted the background and the steady components can be fitted by a power law with  $\alpha = -1.6$  (Torii et al. 1998). Adopting the distance to be 3.3 kpc (Caswell et al. 1975), we can calculate its unabsorbed flux as  $3.1 \times 10^{-12}$  ergs  $\text{cm}^{-2}$   $s^{-1}$ , which yields  $N_{\text{pl}} = 6.5 \times 10^{10} d^2 (r_0/\varpi_{\text{LC}})^{-2}$ . On the other hand, the distance of J0822–4300 was estimated from VLA observations as  $d = 2.2 \pm 0.3$  kpc (Reynoso et al. 1995). *ROSAT* observations revealed that the soft X-ray emission of this pulsar is consistent with a single-temperature blackbody model with  $kT_s = 0.28 \pm 0.10$  keV and  $A_s \sim 0.04 A_*(d/2.2)^2$  (Petre, Becker, & Winkler 1996).

**Vela.**—From *ROSAT* observations in 0.06–2.4 keV, the spectrum of its point-source (presumably the pulsar) emission is expressed by two components: a surface blackbody component with  $kT_s = 150$  eV and  $A_s = 0.066 A_*(d/0.5)^2$  and a power-law component with  $\alpha = -3.3$  (Ögelman, Finley, & Zimmermann 1993). However, the latter component does not show pulsations; therefore, we consider only the former component to be the X-ray field illuminating the outer gap.

**B1951+32.**—From *ROSAT* observations in 0.1–2.4 keV, the spectrum of its point-source (presumably the pulsar) emission can be fitted by a single power-law component with  $\alpha = -1.6$  and intrinsic luminosity of  $2.3 \times 10^{33} (d/2.5)^2$  ergs  $s^{-1}$  (Safi-Harb, Ögelman, & Finley 1995), which yields  $N_{\text{pl}} = 9.1 \times 10^{11} d^2 (r_0/\varpi_{\text{LC}})^{-2}$ . The extension of this power law is consistent with the upper limit of the pulsed component in the 2–10 keV energy band (Saito 1998).

**B1821–24.**—From *ASCA* observations in the 0.7–10 keV band, its pulsed emission subtracted the background and the steady components can be fitted by a power law with  $\alpha = -1.2$  (Saito et al. 1997). The unabsorbed flux in this energy range is  $3.5 \times 10^{-12}$  ergs  $\text{cm}^{-2}$   $s^{-1}$ , which leads to  $N_{\text{pl}} = 1.4 \times 10^{14} d^2 (r_0/\varpi_{\text{LC}})^{-2}$ .

**B0656+14.**—Combining *ROSAT* and *ASCA* data, Greiveldinger et al. (1996) reported that the X-ray spectrum consists of three components: the soft surface blackbody with  $kT_s = 67$  eV and  $A_s = 4.5 A_*(d/0.76)^2$ , a hard blackbody with  $kT_h = 129$  eV and  $A_h = 3.2 \times 10^{-2} A_*(d/0.76)^2$ , and a power law with  $\alpha = -1.5$  and  $N_{\text{pl}} = 3.1 \times 10^5 d^2$ . The hard blackbody component takes the major role in maintaining the gap, by virtue of its large emitting area.

**Geminga.**—The X-ray spectrum consists of two components: the soft surface blackbody with  $kT_s = 50$  eV and  $A_s = 0.22 A_*(d/0.16)^2$  and a hard power law with  $\alpha = -1.6$  and  $N_{\text{pl}} = 3.9 \times 10^6 d^2$  (Halpern & Wang 1997). A parallax distance of 160 pc was estimated from *Hubble Space Telescope* (*HST*) observations (Caraveo et al. 1996).

**B1055–52.**—Combining *ROSAT* and *ASCA* data, Greiveldinger et al. (1996) reported that the X-ray spectrum consists of two components: a soft blackbody with  $kT_s = 68$

eV and  $A_s = 7.3 A_*(d/1.53)^2$  and a hard blackbody with  $kT_h = 320$  eV and  $A_h = 2.3 \times 10^{-4} A_*(d/1.53)^2$ .

**J0437–4715.**—Using *ROSAT* and *Extreme Ultraviolet Explorer* (*EUVE*) data (Becker & Trümper 1993, 1999; Halpern, Martin, & Marshall 1996), Zavlin & Pavlov (1998) demonstrated that both the spectra and the light curves of its soft X-ray radiation can originate from hot polar caps with a nonuniform temperature distribution and be modeled by a steplike function having two different temperatures. The first component is the emission from heated polar cap core with temperature  $kT_h = 10^{6.16}$  K measured at the surface and with an area  $A_h = 5.3 \times 10^{-4} A_*(d/0.180)^2$ . The second one can be interpreted as a cooler rim around the polar cap on the neutron star surface with temperature  $kT_s = 10^{5.53}$  K and with an area  $A_s = 0.16 A_*(d/0.180)^2$ . Considering the gravitational redshift factor of 0.76, the best-fit temperatures observed at infinity become  $kT_s = 22$  eV and  $kT_h = 95$  eV. From parallax measurements, its distance is reported to be  $178 \pm 26$  pc (Sandhu et al. 1997). We adopt  $d = 180$  pc as a representative value.

#### 4.2. Input Infrared Field

We next consider the infrared photon field illuminating the gap. In addition to the references cited below, see also Thompson et al. (1999) for Crab, B1509–58, Vela, B1951+32, Geminga, and B1055–52.

**Crab.**—Interpolating the phase-averaged color spectrum in the UV, U, B, V, R (Percival et al. 1993), J, H, and K (Eikenberry et al. 1997) bands and the radio observation at 8.4 GHz (Moffett & Hankins 1996), the spectrum in the IR energy range can be fitted by a single power law (Fig. 5):

$$\nu F_\nu = 5.75 \times 10^{-5} \nu^{1.12} \text{ Jy Hz}, \quad (41)$$

where  $\nu$  is in hertz. The Crab pulsar's flux at 8.4 GHz is, in fact, very uncertain because it can scintillate away from Earth for tens of minutes to hours. Moffett obtained a value of 0.61 mJy from the profiles he collected, while Frail got a value of  $0.5 \pm 0.1$  mJy from VLA imaging (D. A. Moffett 2000, private communication). They are within  $1\sigma$  (0.1 mJy) of each other. To estimate a conservative infrared photon number, we simply assume that the flux at 8.4 GHz is  $0.6 \pm 0.2$  mJy as a crude estimate, because Moffett & Hankins (1996) previously gave the value of 0.76 mJy. If the

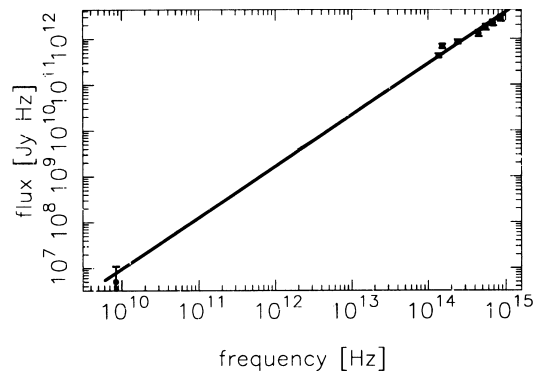


FIG. 5.—Single power-law fit of phase-averaged color spectrum of the Crab pulsar. The abscissa is the photon frequency in hertz, while the ordinate is the photon flux in janskys hertz.



error bar at 8.4 GHz is smaller, then the infrared photon density around 0.01 eV reduces further; this in turn results in a less upscattered, TeV flux. Equation (41) gives the following infrared number spectrum:

$$dN_{\text{IR}}/d\epsilon_{\text{IR}} = 1.5 \times 10^{17} d^2(r_0/\varpi_{\text{LC}})^{-2} \epsilon_{\text{IR}}^{-0.88}, \quad (42)$$

where  $\epsilon_{\text{IR}} m^e c^2$  refers to the infrared photon energy.

**B0540–69.**—Its de-extincted optical and soft X-ray pulsed flux densities can be interpolated as  $F_{\nu} = 0.207\nu^{-0.3}$  Jy (Middleditch & Pennypacker 1985). This line extrapolates to 0.47 mJy at 640 MHz, which is consistent with an observed value 0.4 mJy (Manchester et al. 1993). We thus extrapolate the relation  $F_{\nu} = 0.207\nu^{-0.3}$  to the infrared energies and obtain

$$dN_{\text{IR}}/d\epsilon_{\text{IR}} = 1.6 \times 10^{12} d^2(r_0/\varpi_{\text{LC}})^{-2} \epsilon_{\text{IR}}^{-1.3}. \quad (43)$$

**B1509–58.**—The flux densities emitted from close to the neutron star in radio (Taylor, Manchester, & Lyne 1993), optical (Caraveo, Mereghetti, & Bignami 1994b), soft X-ray (Seward et al. 1984), and hard X-ray (Kawai, Okayasu, & Sekimoto 1993) bands can be fitted by a single power law  $F_{\nu} = 1.36\nu^{-0.32}$  Jy. We thus adopt

$$dN_{\text{IR}}/d\epsilon_{\text{IR}} = 4.7 \times 10^{11} d^2(r_0/\varpi_{\text{LC}})^{-2} \epsilon_{\text{IR}}^{-1.3}. \quad (44)$$

**Vela.**—The flux densities emitted from close to the neutron star in radio (Taylor, Manchester, & Lyne 1993; Downs, Reichley, & Morris 1973) and optical (Manchester et al. 1980) bands can be fitted by  $F_{\nu} = 1.71 \times 10^7 \nu^{-0.91}$  Jy. We thus adopt

$$dN_{\text{IR}}/d\epsilon_{\text{IR}} = 1.8 \times 10^7 d^2(r_0/\varpi_{\text{LC}})^{-2} \epsilon_{\text{IR}}^{-1.9}. \quad (45)$$

**B1951+32.**—The flux densities emitted from close to the neutron star in radio (Taylor, Manchester, & Lyne 1993) and soft X-ray (Safi-Harb, Ögelman, & Finley 1995) bands can be interpolated as  $F_{\nu} = 32.8\nu^{-0.49}$  Jy. We thus adopt

$$dN_{\text{IR}}/d\epsilon_{\text{IR}} = 6.3 \times 10^{10} d^2(r_0/\varpi_{\text{LC}})^{-2} \epsilon_{\text{IR}}^{-1.5}. \quad (46)$$

**B0656+14.**—The nonthermal (most likely, magnetospheric) emission in the *I*, *R*, *V*, and *B* bands shows spectral index  $-1.53$  (Caraveo, Bignami, & Mereghetti 1994a; Kurt et al. 1998), which is much softer than that of Crab (eq. [42]). If we were to extrapolate it to the radio frequency, the flux density at 1 GHz would exceed 100 Jy; therefore, it is likely that the soft power-law spectrum becomes harder below a certain frequency. We thus estimate the upper limit of infrared flux density by interpolating between radio (6 and 4 mJy at 0.4 and 1.4 GHz, respectively; Taylor et al. 1993) and infrared-optical observations (0.71, 0.47, 0.40  $\mu$ Jy at *I*, *R*, *V* bands). The result is

$$dN_{\text{IR}}/d\epsilon_{\text{IR}} = 2.0 \times 10^1 d^2(r_0/\varpi_{\text{LC}})^{-2} \epsilon_{\text{IR}}^{-2.7}. \quad (47)$$

**Geminga.**—The upper limit of the flux density in the radio band (Taylor et al. 1993) and the flux density in the optical band (Shearer et al. 1998) gives spectral index greater (or harder) than  $-0.69$ . Interpolating the infrared flux with these two frequencies, we obtain

$$dN_{\text{IR}}/d\epsilon_{\text{IR}} = 1.9 \times 10^7 d^2(r_0/\varpi_{\text{LC}})^{-2} \epsilon_{\text{IR}}^{-1.7}, \quad (48)$$

which gives a conservative upper limit of infrared photon number density under the assumption of a single power-law interpolation.

**B1055–52.**—The flux densities emitted from close to the neutron star in radio (Taylor et al. 1993) and optical (Mignani, Caraveo, & Bignami 1997) bands can be interpolated as  $F_{\nu} = 4.2 \times 10^5 \nu^{-0.77}$  Jy. We thus adopt

$$dN_{\text{IR}}/d\epsilon_{\text{IR}} = 7.7 \times 10^7 d^2(r_0/\varpi_{\text{LC}})^{-2} \epsilon_{\text{IR}}^{-1.8}. \quad (49)$$

**J1617–5055, J0822–4300, B1821–24, and J0437–4715.**—There have been no available infrared or optical observations for these four pulsars. We thus simply assume that  $\alpha = -1.5$  for these four pulsars and that  $\nu F_{\nu} = 10^9$  Jy Hz at 0.01 eV. We then obtain

$$dN_{\text{IR}}/d\epsilon_{\text{IR}} = 2.5 \times 10^7 d^2(r_0/\varpi_{\text{LC}})^{-2} \epsilon_{\text{IR}}^{-1.5} \quad (50)$$

for J1617–5055, while

$$dN_{\text{IR}}/d\epsilon_{\text{IR}} = 2.1 \times 10^7 d^2(r_0/\varpi_{\text{LC}})^{-2} \epsilon_{\text{IR}}^{-1.5} \quad (51)$$

for J0822–4300,

$$dN_{\text{IR}}/d\epsilon_{\text{IR}} = 1.3 \times 10^{14} d^2(r_0/\varpi_{\text{LC}})^{-2} \epsilon_{\text{IR}}^{-1.5} \quad (52)$$

for B1821–24, and

$$dN_{\text{IR}}/d\epsilon_{\text{IR}} = 3.6 \times 10^{13} d^2(r_0/\varpi_{\text{LC}})^{-2} \epsilon_{\text{IR}}^{-1.5} \quad (53)$$

for J0437–4715.

### 4.3. Curvature-radiated $\gamma$ -Rays

In this subsection, we present the results of GeV emission via curvature process and compare them with observations. The results are presented for the two assumed values of  $\alpha = 30^\circ$  and  $45^\circ$ .

For Crab, B0540–69, B1509–58, and J1617–5055, the X-ray field is dominated by the power-law component, producing high number densities above  $10^{15} \text{ cm}^{-3}$ . In this case, the gap half-widths are less than 10% of  $\varpi_{\text{LC}}$ . The intrinsic luminosities of these young pulsars in the GeV energy range exceed  $10^{33} \text{ ergs s}^{-1}$ . Except for the distant pulsar B0540–69, their GeV fluxes are expected to be large enough to be observed with a space  $\gamma$ -ray telescope.

For the relatively young pulsars J0822–4300 and Vela, the X-ray field is dominated by the surface blackbody component; the number density ( $N_{\text{X}}$ ) becomes about  $10^{14} \text{ cm}^{-3}$ . The gap half-width is about 5% of  $\varpi_{\text{LC}}$ , and the intrinsic GeV luminosity is  $\sim 10^{33} \text{ ergs s}^{-1}$ .

For the middle-aged pulsar B1951+32, its relatively strong magnetic field at the gap center ( $B \sim 10^6 \text{ G}$ ) results in a strong GeV emission like that of the young pulsars.

The millisecond pulsar B1821–24 has a very strong magnetic field ( $B \sim 10^{7.5} \text{ G}$ ) at the gap center. However, its strong ( $N_{\text{X}} \sim 10^{17.5} \text{ cm}^{-3}$ ) X-ray field prevents the gap from extending in the magnetosphere. As a result,  $L_{\text{GeV}}$  is relatively small compared with other pulsars.

For the three middle-aged pulsars B0656+14, Geminga, and B1055–52, their power-law components are too weak to dominate the surface blackbody emissions; the surface emissions are also too weak ( $N_{\text{X}} < 10^{14.2}$ ) to allow the gaps to extend more than 10% of  $\varpi_{\text{LC}}$ . However, the extended gaps do not mean large intrinsic GeV luminosities, because their small magnetic fields ( $B < 10^{4.5} \text{ G}$ ) suppress the acceleration field. In the case of Geminga, its proximity leads to a large GeV flux.

In the case of the millisecond pulsar J0437–4715, its weak X-ray field ( $N_{\text{X}} < 10^{14} \text{ cm}^{-3}$ ) due to the soft and hard

blackbody emissions results in an extended gap. This active gap, together with its proximity, leads to a large GeV flux next to Geminga. However, its relatively strong magnetic field ( $B \sim 10^6$  G) at the gap center may indicate the presence of an additional power-law component, which reduces the gap width and hence the GeV flux. Therefore, further hard X-ray observations are necessary for this millisecond pulsar.

#### 4.4. Invisibility of TeV Pulses

If an electron or a positron is migrating with Lorentz factor  $\Gamma \gg 1$  in an isotropic photon field, it upscatters the soft photons to produce the following number spectrum of  $\gamma$ -rays (Blumenthal & Gould 1970):

$$\frac{d^2N}{dt d\epsilon_\gamma} = \frac{3}{4} \sigma_T \frac{c}{\Gamma^2} \frac{dN_{\text{IR}}}{d\epsilon_{\text{IR}}} \frac{d\epsilon_{\text{IR}}}{\epsilon_{\text{IR}}} \times \left[ 2q \ln q + (1 + 2q)(1 - q) + \frac{(Qq)^2(1 - q)}{2(1 + Qq)} \right], \quad (54)$$

where  $Q \equiv 4\epsilon_{\text{IR}} \Gamma$  and  $q \equiv \epsilon_\gamma / Q(\Gamma - \epsilon_\gamma)$ ; here,  $\epsilon_\gamma$  refers to the energy of the upscattered photons in units of  $m_e c^2$ . Substituting the infrared photon spectrum  $dN_{\text{IR}}/d\epsilon_{\text{IR}}$ , integrating  $d^2N/dt d\epsilon_\gamma$  over  $\epsilon_{\text{IR}}$ , and multiplying the  $\gamma$ -ray energy ( $\epsilon_\gamma m_e c^2$ ) and the electron number ( $N_e$ ) in the gap, we obtain the flux density of the upscattered, TeV photons as a function of  $\epsilon_\gamma$ .

We compute the TeV spectra of individual pulsars and summarize the results in Table 3; the  $\nu F_\nu$  peak frequencies

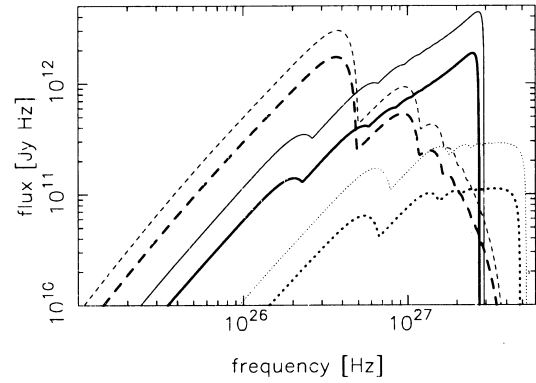


FIG. 6.—Expected TeV spectra of the three brightest pulsars: Crab (solid lines), B0656+14 (dashed lines), and B1509-58 (dotted lines). The thick and thin curves represent the cases of  $\alpha_i = 30^\circ$  and  $45^\circ$ , respectively. The abscissa is the photon frequency in hertz, while the ordinate is the photon flux in janskys hertz.

and the fluxes are given in the last two columns. Moreover, for the three brightest pulsars (Crab, B0656+14, and B1509-58), their computed  $\nu F_\nu$  spectra are presented in Figure 6. It follows from Table 3 and Figure 6 that the TeV emissions are invisible with the current ground-based telescopes, except for Crab and B0656+14. Since  $H$  becomes as small as  $l_{\text{acc}}$  for the Crab pulsar, a significant fraction of the particles are, in fact, unsaturated. Therefore, the expected TeV flux is overestimated. To constrain the absolute pulsed TeV flux from the Crab pulsar, we must discard the mono-

TABLE 3  
EXPECTED  $\gamma$ -RAY PROPERTIES

Pulsar	$\alpha_i$ (deg)	$l_{\text{acc}}/H$	$H/\varpi_{\text{LC}}$	$E_c$ (GeV)	$L_{\text{GeV}}$ (ergs s $^{-1}$ )	$L_{\text{GeV}}/d^2$ (Jy Hz)	$\nu_{\text{peak}}$ (Hz)	$(\nu F_\nu)_{\text{TeV}}^a$ (Jy Hz)
Crab.....	30	0.82	0.023	4.2	$1.3 \times 10^{33}$	$2.1 \times 10^{12}$	$2.5 \times 10^{27}$	$1.9 \times 10^{12}$
	45	0.96	0.016	5.2	$1.8 \times 10^{33}$	$3.0 \times 10^{12}$	$2.7 \times 10^{27}$	$4.4 \times 10^{12}$
B0540-69.....	30	0.21	0.048	7.8	$8.5 \times 10^{33}$	$3.6 \times 10^{10}$	$2.7 \times 10^{27}$	$8.3 \times 10^{10}$
	45	0.24	0.034	9.8	$1.3 \times 10^{34}$	$5.3 \times 10^{10}$	$2.9 \times 10^{27}$	$2.1 \times 10^{11}$
B1509-58.....	30	0.21	0.075	5.1	$5.7 \times 10^{33}$	$3.1 \times 10^{12}$	$3.4 \times 10^{27}$	$1.1 \times 10^{11}$
	45	0.23	0.053	6.6	$9.0 \times 10^{33}$	$4.9 \times 10^{12}$	$3.6 \times 10^{27}$	$2.9 \times 10^{11}$
J1617-5055.....	30	0.093	0.097	8.7	$1.4 \times 10^{34}$	$7.4 \times 10^{12}$	$1.2 \times 10^{27}$	$1.0 \times 10^8$
	45	0.10	0.068	11.1	$2.2 \times 10^{34}$	$1.1 \times 10^{13}$	$2.0 \times 10^{27}$	$2.5 \times 10^8$
J0822-4300.....	30	0.69	0.045	2.5	$5.7 \times 10^{32}$	$1.2 \times 10^{12}$	$6.0 \times 10^{26}$	$1.0 \times 10^7$
	45	0.57	0.035	3.9	$1.4 \times 10^{33}$	$3.1 \times 10^{12}$	$7.6 \times 10^{26}$	$3.7 \times 10^7$
Vela .....	30	0.27	0.084	3.5	$1.7 \times 10^{33}$	$7.0 \times 10^{13}$	$3.2 \times 10^{26}$	$8.4 \times 10^{10}$
	45	0.26	0.062	4.9	$3.3 \times 10^{33}$	$1.4 \times 10^{14}$	$4.0 \times 10^{26}$	$2.6 \times 10^{11}$
B1951+32.....	30	0.16	0.092	5.4	$2.8 \times 10^{33}$	$4.7 \times 10^{12}$	$6.3 \times 10^{26}$	$3.1 \times 10^{10}$
	45	0.18	0.064	6.9	$4.2 \times 10^{33}$	$7.1 \times 10^{12}$	$7.4 \times 10^{26}$	$8.0 \times 10^{10}$
B1821-24.....	30	0.22	0.067	5.2	$4.6 \times 10^{32}$	$1.8 \times 10^{11}$	$5.0 \times 10^{26}$	$6.2 \times 10^7$
	45	0.25	0.047	6.7	$7.2 \times 10^{32}$	$2.9 \times 10^{11}$	$4.7 \times 10^{26}$	$1.6 \times 10^8$
B0656+14.....	30	0.43	0.160	1.1	$2.0 \times 10^{32}$	$3.7 \times 10^{12}$	$3.7 \times 10^{26}$	$1.7 \times 10^{12}$
	45	0.69	0.098	1.2	$1.8 \times 10^{32}$	$3.2 \times 10^{12}$	$3.8 \times 10^{26}$	$3.0 \times 10^{12}$
Geminga <sup>b</sup> .....	30	0.059	0.334	4.0	$4.1 \times 10^{33}$	$1.7 \times 10^{15}$	$1.5 \times 10^{27}$	$7.0 \times 10^9$
	45	0.083	0.213	4.5	$4.3 \times 10^{33}$	$1.8 \times 10^{15}$	$6.5 \times 10^{26}$	$1.4 \times 10^{10}$
B1055-52 <sup>b</sup> .....	30	0.62	0.130	0.98	$8.5 \times 10^{31}$	$3.8 \times 10^{11}$	$6.0 \times 10^{26}$	$6.3 \times 10^9$
	45	1.0 <sup>c</sup>	0.078	1.0	$7.1 \times 10^{31}$	$3.2 \times 10^{11}$	$6.0 \times 10^{26}$	$1.1 \times 10^{10}$
J0437-4715.....	30	0.043	0.371	5.0	$6.1 \times 10^{32}$	$2.0 \times 10^{14}$	$6.3 \times 10^{26}$	$5.1 \times 10^7$
	45	0.062	0.233	5.4	$6.1 \times 10^{32}$	$2.0 \times 10^{14}$	$5.9 \times 10^{26}$	$9.9 \times 10^7$

<sup>a</sup> The TeV fluxes are evaluated at the  $\nu F_\nu$  peak frequency,  $\nu_{\text{peak}}$ .

<sup>b</sup> The entries for these two pulsars are in italics because their predicted  $\gamma$ -ray properties cannot explain the observations well. See § 5.6 for details.

<sup>c</sup> The Lorentz factors are assumed to be the value that can be attained if particles are accelerated by  $\bar{E}_\parallel$  in length  $H$ .

energetic approximation for the particle distribution function and explicitly solve the Boltzmann equations of particles and  $\gamma$ -rays, together with the Poisson equation for  $\Phi$ , under suitable boundary conditions. In addition, considering the fact that the tertiary infrared photons are not isotropic but have small collision angles with the particles, we can understand that the TeV fluxes computed from equation (54) are, in general, overestimated. For B1055–52 and B0656+14, the emitting areas of the soft blackbody components are unnaturally large. Therefore, more accurate X-ray observations are necessary for a quantitative prediction of their TeV fluxes.

It is worth noting that the TeV fluxes are less than 3% of the GeV fluxes except for Crab, B0540–69, and B0656+14; this conclusion is qualitatively consistent with Romani (1996). The predicted TeV flux from B0540–69 is greater than the GeV flux because (for  $\alpha_i = 30^\circ$  for instance) its infrared photon number density in the energy interval 0.01 and 0.1 eV attains  $7.5 \times 10^{18} \text{ cm}^{-3}$ , which well exceeds the X-ray number density  $6.4 \times 10^{17} \text{ cm}^{-3}$  between 0.1 and 100 keV.

## 5. DISCUSSION

### 5.1. Summary

To sum up, we have considered the electrodynamic structure of an outer gap accelerator in which relativistic particles emit  $\gamma$ -rays via a curvature process. Imposing the gap closure condition that a single pair produces one pair in the gap on average, we solve self-consistently the gap width as a function of the X-ray fields and the pulsar parameters. Once the gap width is known, we can further compute the acceleration field and the resultant  $\gamma$ -ray emissions. It was demonstrated that the luminosities of GeV and TeV emissions are a decreasing function of the X-ray energy and number density. We also showed that the expected  $\nu F_\nu$  fluxes ( $< 10^{11.5} \text{ Jy Hz}$ ) of IC-scattered, TeV  $\gamma$ -rays from the outer gaps of rotation-powered pulsars are less than the observational upper limits, except for Crab and B0656+14. For Crab, an energy-dependent particle distribution function should be considered, whereas, for B0656+14, more accurate X-ray observations are required. It is concluded that the difficulty of excessive TeV emission, which appears in the CHR picture, does not arise in the present outer gap model.

### 5.2. Stability of the Gap

The outer gap in the present model is stable, regardless of whether the X-ray field is dominated by a surface blackbody or a magnetospheric power-law component. Consider the case when the gap width  $H$  slightly increases as an initial perturbation. It increases both  $E_\parallel$  and  $V_{\text{gap}}$ , which in turn increases both  $E_c$  and  $N_\gamma$ . The increase of  $E_c$  results in the decrease of  $E_{\text{th}}$ .

1. When the surface blackbody dominates the X-ray field, the X-ray spectrum and luminosity are unchanged by the perturbation. Therefore, the decrease of  $E_{\text{th}}$  implies the decrease of  $\lambda_1$  or  $\lambda_2$  and hence  $\lambda_p$ .

2. When the magnetospheric emission dominates, the secondary and tertiary emissions will increase with  $E_c$  and  $N_\gamma$ ; therefore,  $N_{\text{pl}}$  increases as well. Accordingly, the decrease of  $E_{\text{th}}$  and the increase of  $N_{\text{pl}}$  imply a significant decrease of  $\lambda_3$  and hence  $\lambda_p$ . In either case, it follows that  $\lambda_p$

decreases owing to the initial increase of  $H$ . Recalling the gap closure condition  $H = \lambda_p/N_\gamma$ , we find a negative feedback that cancels the initial perturbation of  $H$ .

### 5.3. Pulse Sharpness

Let us discuss the expected sharpness of GeV pulses. It seems unlikely that the azimuthal width of the gap increases with decreasing  $H$ . Therefore, it would be possible to argue that the solid angle in which the primary  $\gamma$ -rays are emitted decreases as the arc of the gap along the last open field line (i.e.,  $2H$ ) decreases. On these grounds, we can expect a sharp pulse when  $h \ll 1$  holds, such as for Crab and J0822–4300.

Qualitatively speaking, the same conclusion can be expected for millisecond pulsars and magnetars. In the case of a millisecond pulsar, its fast rotation shrinks the light cylinder. In such a small-volume magnetosphere, the outer gap is immersed in a dense magnetospheric, power-law X-ray emission. As a result,  $\lambda_p$  decreases to reduce  $h$ . In the case of a magnetar, its strong magnetic field makes the expansion coefficient  $A$  in equation (2) be large. Therefore, a very thin ( $h \ll 1$ ) gap with a strong  $E_\parallel$  would be expected. In short, for young pulsars, millisecond pulsars, and magnetars, their high-energy pulsations are expected to show sharp peaks.

### 5.4. Validity of Assumptions

First, we reduced the Poisson equation to one-dimensional form (eq. [2]), by assuming  $D_\perp \gg H$ . Let us briefly consider the two-dimensional effect due to the transverse derivative in the Poisson equation. When  $D_\perp$  becomes small, the gap shifts outward,  $E_\parallel$  is partially screened, and  $H$  enlarges (Fig. 12 in Paper I; see also Cheng, Ho, & Ruderman 1986a for a screened, or spatially constant  $E_\parallel$  in a thin gap). Owing to the screened acceleration field, the GeV and TeV fluxes become small compared with those obtained in the  $D_\perp \gg H$  case. On these grounds, we can constrain the upper limit of the TeV fluxes in the transversely thick limit,  $D_\perp \gg H$ .

Second, let us discuss the case when the assumption of the vacuum gap breaks down. In this case, the charges in the gap partially cancel the original  $E_\parallel$  obtained in the vacuum gap (eq. [2]). The partially screened  $E_\parallel$  results in the decrease of the TeV fluxes. On these grounds, we can regard the TeV fluxes presented in the present paper as the firm upper limits.

Third, we consider the influence of cyclotron resonance scatterings. For one thing, the *soft* blackbody emission from the whole surface may be scattered to be anisotropic (Daugherty & Harding 1989). Such effects are important for polar cap models, because the collision angles ( $\cos^{-1} \mu_c$ ) suffer significant corrections. Nevertheless, in an outer gap, such corrections are negligibly small. Moreover, the cyclotron resonance increases the effective emitting area and decreases the temperature. For simplicity, we neglect these two effects in this paper, because they cancel each other. For example, the decreased temperature results in a decrease of the target photons above a certain threshold energy for pair production. On the other hand, the increased emitting area increases the number of target photons above the threshold, thereby canceling the effect of the decreased temperature. What is more, the *hard* blackbody emission from the heated

polar caps may be scattered to be smeared out. That is, most of the hard X-rays may be scattered back to the stellar surface owing to cyclotron resonance scatterings and re-emitted as soft X-rays (Halpern & Ruderman 1993). In this case, the hard component will be indistinguishable from the original soft component due to the neutron star cooling. Nevertheless, for older pulsars such as B0656+14 and B1055-52, this effect seems to be ineffective probably because of their less dense electrons around the polar cap near the neutron star surface.

### 5.5. $\gamma$ -Ray Luminosity versus Spin-down Luminosity

Curvature-radiated luminosity,  $L_{\text{GeV}}$ , has a weak dependence on the spin-down luminosity,  $L_{\text{spin}}$ , if we fix the trans-field thickness of the gap,  $D_{\perp}/\varpi_{\text{LC}}$ . In other words, the evolution of  $D_{\perp}/\varpi_{\text{LC}}$  is crucial to discussing the  $L_{\text{GeV}} \propto L_{\text{spin}}^{0.5}$  relation (Thompson et al. 1994; Nel et al. 1996). To solve  $D_{\perp}$ , we must analyze the two-dimensional Poisson equation on the poloidal plane; however, this is beyond the scope of the present paper.

### 5.6. Limitation of the Vacuum-Gap Approximation

We now discuss the two pulsars whose predicted  $\gamma$ -ray properties are shown in *italics* in Table 3. For Geminga, its large size  $h$  ( $\sim 0.3$ ) seems to indicate broad pulses. However, its  $\gamma$ -ray pulses are known to be sharp; their fractional phase width is about 0.12 (Mayer-Hasselwander et al. 1994; Mattox, Halpern, & Caraveo 1998; Fierro et al. 1998). Moreover, its GeV flux ( $\sim 10^{15}$  Jy Hz) is more than several hundred times greater than that of the Crab pulsar, which is not observed. We consider these discrepancies to be due to our oversimplified assumption of the vacuum gap. Extending the method presented in Papers I, II, and III, in which the Vlasov equations are solved, to the case when electrons enter from the outer boundary of the gap, we preliminarily find that the nonvacuum gap shifts inward (starward). For example, if the electron influx at the outer boundary attains 20% of the local Goldreich-Julian value, the gap roughly shifts to the middle point between the star surface and  $(r_0, \theta_0)$ , where the vacuum gap would reside. In this case,  $h$  reduces about 3 times and  $L_{\text{GeV}}$  about 30 times; it is preferable to account for the observations.

As for B1055-52, we consider its broad pulses in X-ray and  $\gamma$ -ray bands to be more naturally explained by an extended gap, which will be realized when positrons enter from the inner (starward) boundary. If the positron influx is comparable to the local Goldreich-Julian value, the gap approaches the light cylinder; in this case, both  $h$  and  $L_{\text{GeV}}$  increase a few times. We will investigate such nonvacuum gaps in a separate paper.

### 5.7. Synchrotron Radiation Below 10 MeV Energies

As we have seen, the accelerated particles reach a curvature-radiation-reaction limit to become roughly monoenergetic. The curvature spectrum in lower energies then becomes a power law with a spectral index  $\frac{1}{3}$ , which is much harder than the observed  $\gamma$ -ray pulsar spectra. In this subsection, we demonstrate that the  $\gamma$ -ray spectrum below a certain energy (say 10 MeV) is dominated by a synchrotron radiation from freshly born particles and that the expected  $\gamma$ -ray spectra further soften.

As an example exhibiting a soft power-law  $\gamma$ -ray spectrum from eV to GeV energies, we consider the Crab pulsar.

To discriminate whether a curvature or synchrotron process dominates, we separately consider each process and take the ratio of the radiation-reaction forces. That is, we ignore much complicated synchrocurvature process, because such details are not important for the present purpose.

Let us first consider the case of  $\alpha_i = 45^\circ$ , which gives  $B_5 = 6.5 \times 10^2$  at the gap center. Since the curvature-radiated  $\gamma$ -ray energy is  $E_c = 5.2$  GeV, the freshly born particles have Lorentz factors of  $\Gamma_0 \sim 5 \times 10^3$ . A particle with this Lorentz factor emits synchrotron radiation around the energy

$$h\nu_{\text{sync}} = \frac{3h\Gamma_0^2 eB \sin \chi_p}{4\pi m_e c}, \quad (55)$$

where  $\chi_p$  denotes the pitch angle of the particles.

We can solve the evolution of the Lorentz factor and  $\chi_p$  simultaneously by the method described in § 5.3 of Paper I. We present the evolution of  $\sin \chi_p$  due to synchrotron radiation shortly after the pair production in Figure 7, and the evolution of the longitudinal momenta in Figure 8. In both figures, the abscissa designates the distance along the field lines in units of  $\varpi_{\text{LC}}$  with respect to the birth place (distance = 0). The particles are supposed to be created with

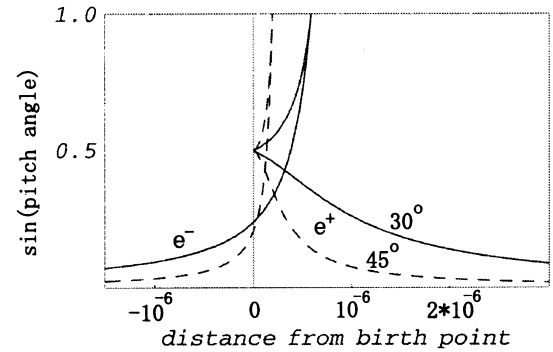


FIG. 7.—Pitch-angle evolution due to synchrotron radiation as a function of position. The abscissa denotes the distance (in units of  $\varpi_{\text{LC}}$ ) along the field lines from the birth place (distance = 0). The thick and thin lines correspond to  $\alpha_i = 30^\circ$  and  $\alpha_i = 45^\circ$ , respectively.

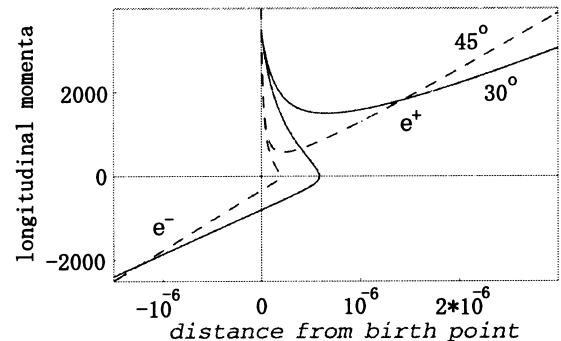


FIG. 8.—Longitudinal momentum evolution due to synchrotron radiation as a function of position. The ordinate is normalized in units of  $m_e c^2$ . The abscissa and the lines are the same as in Fig. 7.

positive momenta; therefore, electrons turn back to have negative longitudinal momenta. Positrons lose longitudinal momenta at the initial stage of acceleration because the relativistic beaming effect causes the synchrotron radiation–reaction force not only in the transverse but also in the longitudinal directions.

It follows from Figure 7 that we can approximate  $\sin \chi_0 \sim 0.3$  when the particles have not run  $\Delta l \sim 1 \times 10^{-6} \varpi_{LC}$  for  $\alpha_i = 45^\circ$ . When  $\chi_p$  is kept around 0.3, Lorentz factors are also of the same order of  $\Gamma_0$ . Substituting  $\sin \chi_p = 0.3$  and  $\Gamma_0 \sim 5 \times 10^3$  into equation (55), we obtain  $h\nu_{\text{sync}} \sim 8.5$  MeV as the central energy of the synchrotron spectrum for  $\alpha_i = 45^\circ$ . The fraction of the particles having  $\sin \chi_p \sim 0.3$  and Lorentz factor  $\sim \Gamma_0$  compared with the saturated particles then becomes

$$\frac{\Delta N_e}{N_e} \sim \frac{\Delta l}{H} \sim 6 \times 10^{-5}. \quad (56)$$

We can estimate the ratio between the synchrotron radiation from the freshly born particles and the curvature radiation from the saturated particles as follows:

$$R_{\text{sc}}(\nu) = \frac{\Delta N_e}{N_e} \frac{dP_{\text{sync}}/d\nu}{dP_{\text{curv}}/d\nu}, \quad (57)$$

where

$$\frac{dP_{\text{sync}}}{d\nu} \equiv \frac{\sqrt{3}e^3 B \sin \chi_0}{m_e c^2} F\left(\frac{h\nu}{h\nu_{\text{sync}}}\right), \quad (58)$$

$$\frac{dP_{\text{curv}}}{d\nu} \equiv \frac{\sqrt{3}e^2 \Gamma}{R_c} F\left(\frac{h\nu}{E_c}\right), \quad (59)$$

and

$$F(x) \equiv x \int_x^\infty K_{5/3}(y) dy; \quad (60)$$

$K_{5/3}$  refers to the modified Bessel function of 5/3 order;  $\Gamma$  in equation (59) denotes the saturated Lorentz factor and becomes  $2.4 \times 10^7$  for  $45^\circ$  for Crab. At the synchrotron peak energy,  $0.29h\nu_{\text{sync}} = 2.5$  MeV, the ratio becomes  $R_{\text{sc}} = 12$ .

In the same manner we can consider the case of  $\alpha_i = 30^\circ$ . In this case, we have  $h\nu_{\text{sync}} \sim 1.7$  MeV and  $\Delta N_e/N_e \sim 1 \times 10^{-4}$ . As a result, we obtain  $R_{\text{sc}} = 11$  at 0.5 MeV.

We can therefore conclude that the  $\gamma$ -ray spectrum below a certain energy ( $\sim 10$  MeV) is dominated by the synchrotron radiation from freshly born particles.

In addition, in the case of Crab, the unsaturated motion of particles ( $l_{\text{acc}} \sim H$ ) implies that the synchrocurvature radiation from unsaturated particles is also important. Therefore, the spectrum below GeV will become much softer compared with the simple curvature spectrum with central energy  $E_c = 5.2$  (or 4.2) GeV for  $\alpha_i = 45^\circ$  (or  $30^\circ$ ).

### 5.8. Comparison with Zhang & Cheng Model

Finally, we point out the difference between the present work and that of Zhang & Cheng (1997); they considered a gap closure condition so that the curvature-radiated  $\gamma$ -ray energy may be adjusted just above the threshold of pair production. That is, they considered the  $\gamma$ -ray energy to be about  $E_{\gamma, \text{ZC}} \equiv (m_e c^2)^2/E_X$ , where  $E_X$  refers to the character-

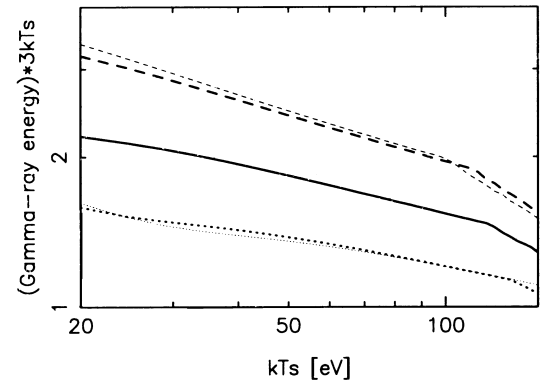


FIG. 9.—Ratio between  $E_c$  computed from eq. (13) and  $E_{\gamma, \text{ZC}}$  (see text). Neither the hard blackbody nor the power-law components are considered. X-rays are supplied by the whole surface blackbody emission; the abscissa refers to the temperature,  $kT_s$ .

istic X-ray energy. By equating  $E_{\gamma, \text{ZC}}$  with the central energy of curvature radiation (eq. [14] in our notation), they closed the equations. When the soft (or hard) blackbody emission dominates,  $E_X$  can be approximated by  $3kT_s$  (or  $3kT_h$ ).

The model of Zhang & Cheng (1997) is, in fact, qualitatively consistent with our gap closure condition, provided that the X-rays are supplied by the soft or hard blackbody emission. More specifically, our model gives about 2 times larger characteristic  $\gamma$ -ray energy compared with their model. To see this, we present in Figure 9 the ratio between  $E_c$  computed from equation (14) and  $E_{\gamma, \text{ZC}}$ ; the hard blackbody or the power-law components are not considered in this calculation. The abscissa indicates the soft blackbody temperature,  $kT_s$ . For the three thick curves,  $\Omega_2$  is fixed at 0.5; the solid, dashed, and dotted lines correspond to  $\mu_{30} = 1.0, 3.0$ , and 0.3, respectively. For the two thin curves, on the other hand,  $\mu_{30}$  is fixed at 1.0; the dashed and dotted curves correspond to  $\Omega_2 = 1.0$  and 0.25, respectively. At small  $kT_s$ , our model gives more than twice greater  $\gamma$ -ray energy compared with that of Zhang & Cheng (1997); nevertheless, the difference is not very prominent.

It should be noted, however, that the spectra of the X-ray radiation are explicitly considered in our present model in the sense we perform the integration over X-ray energies in equations (16), (21), and (25) and that the additional, power-law component is considered in our present model.

It would be interesting to investigate the back-reaction of the accelerated particles on the polar cap heating, which was deeply investigated by Zhang & Cheng (1997). Consider the case when the voltage drop in the gap approaches the surface EMF,  $V_*$ . Such an active gap will supply copious relativistic primary particles to heat up the polar cap because of bombardment. The resultant hard blackbody emission supplies target photons for pair production to make the realistic solution deviate from the thick solid curve and approach thin curves at small  $kT_s$  (Fig. 2). Therefore, this sort of back-reaction on the X-ray field due to the relativistic particles needs further consideration.

This research owes much to the helpful comments of S. Shibata. The author wishes to express his gratitude to Y. Saito, A. Harding, and the anonymous referee for valuable advice. He also thanks the Astronomical Data Analysis Center of the National Astronomical Observatory, Japan, for the use of workstations.

## REFERENCES

- Aschenbach, B., & Brinkmann, W. 1975, *A&A*, 41, 147
- Becker, W., & Trümper, J. 1993, *Nature*, 365, 528
- Becker, W., & Trümper, J. 1999, *A&A*, 341, 803
- Bereetskii, V. B., Lifshitz, E. M., & Pitaevskii, L. P. 1989, *Quantum Electrodynamics*, Landau Lifshitz Course of Theoretical Physics, Vol. 4 (2d ed.; Oxford: Pergamon), § 89
- Blandford, R. D., & Levinson, A. 1995, *ApJ*, 441, 79
- Blumenthal, G. R., & Gould, R. J. 1970, *Rev. Mod. Phys.*, 42, 237
- Bowden, C. C. G., et al. 1993, *Proc. 23d Int. Cosmic-Ray Conf. (Calgary)*, 1, 294
- Caraveo, P. A., Bignami, G. F., & Mereghetti, S. 1994a, *ApJ*, 422, L87
- Caraveo, P. A., Bignami, G. F., Mignani, R., & Taff, L. G. 1996, *ApJ*, 461, L91
- Caraveo, P. A., Mereghetti, S., & Bignami, G. F. 1994b, *ApJ*, 423, L125
- Caswell, J. L., Murray, J. D., Roger, R. S., Cole, D. J., & Cooke, D. J. 1975, *A&A*, 45, 239
- Cheng, K. S. 1994, in *Toward a Major Atmospheric Cerenkov Detector III*, ed. T. Kifune (Tokyo: Universal Academy), 25
- Cheng, K. S., Ho, C., & Ruderman, M. 1986a, *ApJ*, 300, 500
- . 1986b, *ApJ*, 300, 522
- Chiang, J., & Romani, R. W. 1992, *ApJ*, 400, 629
- Chiang, J., & Romani, R. W. 1994, *ApJ*, 436, 754
- Daishido, T. 1975, *PASJ*, 27, 181
- Daugherty, J. K., & Harding, A. K. 1982, *ApJ*, 252, 337
- . 1989, *ApJ*, 336, 861
- . 1996, *ApJ*, 458, 278
- Dermer, C. D., & Sturmer, S. J. 1994, *ApJ*, 420, L75
- Downs, G. S., Reichley, P. E., & Morris, G. A. 1973, *ApJ*, 181, L143
- Edwards, P. G., et al. 1994, *A&A*, 291, 468
- Eikenberry, S. S., Fazio, G. G., Ransom, S. M., Middleditch, J., Kristaian, J., & Pennypacker, C. R. 1997, *ApJ*, 477, 465
- El-Gowhari, A., & Arponen, J. 1972, *Nuovo Cimento*, 11B, 201
- Fierro, J. M., Michelson, P. F., Nolan, P. L., & Thompson, D. J. 1998, *ApJ*, 494, 734
- Gil, J. A., & Krawczyk, A. 1997, *MNRAS*, 285, 561
- Greenstein, G., & Hartke, G. J. 1983, *ApJ*, 271, 283
- Greiveldinger, C., Camerini, U., Fry, W., Markwardt, C. B., Ögelman, H., Safi-Harb, S., Finley, J. P., & Tsuruta, S. 1996, *ApJ*, 465, L35
- Halpern, J. P., Martin, C., & Marshall, H. L. 1996, *ApJ*, 462, 908
- Halpern, J. P., & Ruderman, M. A. 1993, *ApJ*, 415, 286
- Halpern, J. P., & Wang, Y. H. 1997, *ApJ*, 477, 905
- Hardee, P. E., & Rose, W. K. 1974, *ApJ*, 194, L35
- Harding, A. K., Tademaru, E., & Esposito, L. S. 1978, *ApJ*, 225, 226
- Hirotani, K. 2000a, *MNRAS*, 317, 225 (Paper IV)
- . 2000b, *PASJ*, 52, 645
- Hirotani, K., & Shibata, S. 1999a, *MNRAS*, 308, 54 (Paper I)
- . 1999b, *MNRAS*, 308, 67 (Paper II)
- . 1999c, *PASJ*, 51, 683 (Paper III)
- Kanbach, G., et al. 1994, *A&A*, 289, 855
- Kaspi, V. M., Lackey, J. R., Manchester, R. N., Bailes, M., & Pace, R. 2000, *ApJ*, 528, 445
- Kawai, N., Okayasu, R., & Sekimoto, Y. 1993, in *AIP Conf. Proc. 280, Compton Gamma-Ray Observatory*, ed. M. Friedlander, N. Gehrels, & D. J. Macomb (New York: AIP), 213
- Kifune, T. 1996, *Space Sci. Rev.*, 75, 31
- Knight, F. K. 1982, *ApJ*, 260, 538
- Krause-Polstoff, J., & Michel, F. C. 1985a, *MNRAS*, 213, 43P
- . 1985b, *A&A*, 144, 72
- Kundt, W., & Schaaf, R. 1993, *Ap&SS*, 200, 251
- Kurt, V. G., Sokolov, V. V., Zharikov, S. V., Pavlov, G. G., & Komberg, B. V. 1998, *A&A*, 333, 547
- Manchester, R. N., Mar, D. P., Lyne, A. G., Kaspi, V. M., & Johnston, S. 1993, *ApJ*, 403, L29
- Manchester, R. N., Wallace, P. T., Peterson, B. A., & Elliott, K. H. 1980, *MNRAS*, 190, 9P
- Mattox, J. R., Halpern, J. P., & Caraveo, P. A. 1998, *ApJ*, 493, 891
- Mayer-Hasselwander, H. A., Bertsch, D. L., Brazier, T. S., Chiang, J., Fichtel, C. E., Fierro, J. M., Hartman, R. C., & Hunter, S. D. 1994, *ApJ*, 421, 276
- Middleditch, J., & Pennypacker, C. 1985, *Nature*, 313, 659
- Mignani, R., Caraveo, P. A., & Bignami, G. F. 1997, *ApJ*, 474, L51
- Miyazaki, J., & Takahara, F. 1997, *MNRAS*, 290, 49
- Moffett, D. A., & Hankins, T. H. 1996, *ApJ*, 468, 779
- Nel, H. I., Arzoumanian, Z., Bailes, M., Brazier, K. T. S., D'Amico, N., Esposito, J. A., Fichtel, C. E., & Fierro, J. M. 1996, *ApJ*, 465, 898
- Nel, H. I., et al. 1993, *ApJ*, 418, 836
- Nolan, P. L., et al. 1993, *ApJ*, 409, 697
- . 1996, *A&AS*, 120, 61
- Ochelkov, Yu. P., & Usov, V. V. 1980a, *Ap&SS*, 69, 439
- . 1980b, *Soviet Astron. Lett.*, 6, 414
- Ögelman, H., Finley, J. P., & Zimmermann, H. U. 1993, *Nature*, 361, 136
- Pavlov, G. G., Shibano, Yu. A., Ventura, J., & Zavlin, V. E. 1994, *A&A*, 289, 837
- Percival, J. W., et al. 1993, *ApJ*, 407, 276
- Petre, R., Becker, C. M., & Winkler, P. F. 1996, *ApJ*, 465, L43
- Ramanamurthy, P. V., Fichtel, C. E., Kniffen, D. A., Sreekumar, P., & Thompson, D. J. 1996, *ApJ*, 458, 755
- Ramanamurthy, P. V., et al. 1995, *ApJ*, 447, L109
- Reynoso, E. M., Dubner, G. M., Goss, W. M., & Arnal, E. M. 1995, *AJ*, 110, 318
- Romani, R. W. 1987, *ApJ*, 313, 718
- . 1996, *ApJ*, 470, 469
- Romani, R. W., & Yadigaroglu, I. A. 1995, *ApJ*, 438, 314
- Safi-Harb, S., Ögelman, H., & Finley, J. P. 1995, *ApJ*, 439, 722
- Saito, Y. 1998, Ph.D. thesis, Univ. Tokyo
- Saito, Y., Kawai, N., Shibata, S., Dotani, T., & Kulkarni, S. R. 1997, *ApJ*, 477, L37
- Sandhu, J. S., et al. 1997, *ApJ*, 478, L95
- Scharlemann, E. T., Arons, J., & Fawley, W. T. 1978, *ApJ*, 222, 297
- Seward, F. D., Harnden, F. R., Szymkowiak, A., & Swank, J. 1984, *ApJ*, 281, 650
- Shearer, A., et al. 1998, *A&A*, 335, L21
- Shibanov, Yu. A., Zavlin, V. E., Pavlov, G. G., Ventura, J. 1992, *A&A*, 266, 313
- Shibata, S., Miyazaki, J., & Takahara, F. 1998, *MNRAS*, 295, L53
- Sturmer, S. J., Dermer, C. D., & Michel, F. C. 1995, *ApJ*, 445, 736
- Taylor, J. H., Manchester, R. N., & Lyne, A. G. 1993, *ApJS*, 88, 529
- Thompson, D. J., Bailes, M., Bertsch, D. L., Esposito, J. A., Fichtel, C. E., Harding, A. K., Hartman, R. C., & Hunter, S. D. 1996, *ApJ*, 465, 385
- Thompson, D. J., et al. 1994, *ApJ*, 436, 229
- . 1999, *ApJ*, 516, 297
- Torii, K., et al. 1998, *ApJ*, 494, L207
- Ulmer, M. P. 1994, *ApJS*, 90, 789
- Usov, V. V. 1994, *ApJ*, 427, 394
- Yoshikoshi, T., et al. 1997, *ApJ*, 487, L65
- Zavlin, V. E., & Pavlov, G. G. 1998, *A&A*, 329, 583
- Zavlin, V. E., Pavlov, G. G., Shibanov, Yu. A., & Ventura, J. 1995a, *A&A*, 297, 441
- Zavlin, V. E., Shibanov, Yu. A., & Pavlov, G. G. 1995b, *Astron. Lett.*, 21, 149
- Zhang, L., & Cheng, K. S. 1997, *ApJ*, 487, 370